

2010

# Integrated Bioassays for Screening Chemical and Biological Species

Baozhen Chen  
*Iowa State University*

Follow this and additional works at: <https://lib.dr.iastate.edu/etd>

 Part of the [Electrical and Computer Engineering Commons](#)

## Recommended Citation

Chen, Baozhen, "Integrated Bioassays for Screening Chemical and Biological Species" (2010). *Graduate Theses and Dissertations*. 11859.

<https://lib.dr.iastate.edu/etd/11859>

This Dissertation is brought to you for free and open access by the Iowa State University Capstones, Theses and Dissertations at Iowa State University Digital Repository. It has been accepted for inclusion in Graduate Theses and Dissertations by an authorized administrator of Iowa State University Digital Repository. For more information, please contact [digirep@iastate.edu](mailto:digirep@iastate.edu).

# **Integrated bioassays for screening chemical and biological species**

By

**Baozhen Chen**

A dissertation submitted to the graduate faculty  
in partial fulfillment of the requirements for the degree of

**DOCTOR OF PHILOSOPHY**

Major: Electrical Engineering

Program of Study Committee:  
Santosh Pandey, Major Professor

Liang Dong

Jiming Song

Sumit Chaudhary

Jaeyoun Kim

Iowa State University

Ames, Iowa

2010

Copyright © Baozhen Chen, 2010. All rights reserved.

To my beloved Mom and Dad

## Table of Content

List of Figures .....	v
Abstract .....	ix
Chapter 1: Scalable, CMOS-compatible Floating-gate FET for Detection of Charged Biochemical Molecules.....	1
1.1 Introduction .....	1
1.1.1 Ion Selective FET.....	2
1.1.2 Chemoreceptive Neuron MOS .....	3
1.2 Proposed Umbrella-Shaped Field Effect Transistor (UGFET) .....	4
1.3 UGFET Design and Analysis .....	5
1.4 UGFET Fabrication .....	9
1.5 Experimental Results.....	10
1.5.1 Electrical Characterization .....	11
1.5.2 Transconductance Measurement .....	12
1.5.3 Subthreshold Measurement .....	15
1.6 Discussion .....	17
Chapter 2: MEMS Bioassay for Characterizing Nematode Phenotype .....	19
2.1 Introduction .....	19
2.2 Device Design and Analysis.....	22
2.2.1 Fabrication of Microfluidic Devices .....	22
2.2.2 Sample and Medium Preparation .....	23
2.2.3 <i>O. dentatum</i> Larvae as Test Nematodes .....	24
2.2.4 Data Capture and Analysis .....	24
2.2.5 Calculation of Locomotion Parameters .....	25
2.3 Experimental Results.....	28
2.3.1 Amplitude Measurements.....	28
2.3.2 Wavelength Measurements .....	29
2.3.3 Tangential Force for Forward Movement .....	31
2.3.4 Velocity Measurements.....	34
2.3.5 Frequency Measurements.....	36
2.3.6 Worm Image Tracking Program.....	37

2.4 Discussion .....	40
Chapter 3: Automated Screening of Nematodes in Sinusoidal Microfluidic Channels .....	44
3.1 Introduction .....	44
3.2 Fixed Sine-wave Devices .....	46
3.2.1 Sinusoidal Channel Designs .....	46
3.2.2 Device Fabrication .....	50
3.2.3 <i>O. dentatum</i> Larvae as Test Nematodes .....	51
3.2.4 Sample Preparation and Loading.....	52
3.2.5 Data Capture and Analysis .....	52
3.2.6 Calculation of Locomotion Parameters .....	53
3.2.7 Experimental Results.....	54
3.3 Frequency Modulated (FM) Sine-wave Channels.....	57
3.3.1 FM Channel Designs .....	57
3.3.2 Device Fabrication .....	59
3.3.3 Extraction of Locomotion Parameters.....	60
3.3.4 Experimental Results.....	61
3.4 Amplitude Modulated (AM) Sine-wave Channels .....	65
3.4.1 AM Channel Designs .....	65
3.4.2 Device Fabrication, Experimental Protocols and Data Analysis.....	66
3.4.3 Experimental Results.....	67
3.5 Discussion .....	71
Chapter 4: Conclusions and Future Scope .....	74
References.....	76
Appendix 1: Image-tracking Software.....	81
Appendix 2: Mask Designs for Sine-wave Channels .....	86
Appendix 3: Publications and Awards.....	90
Acknowledgements.....	92

## List of Figures

<b>Figure 1.1:</b> Schematic views of a MOSFET (a) and ISFET (b) .....	3
<b>Figure 1.2:</b> Illustration of a CvMOS transistor.....	4
<b>Figure 1.3:</b> (a) Cross-section of the proposed UGFET and its symbolic representation with an equivalent capacitance model (b) .....	5
<b>Figure 1.4:</b> Three-dimensional UGFET cross-section built with the Synopsis device simulator. ....	7
<b>Figure 1.5:</b> Three-dimensional electrical potential distribution of UGFET using Sentaurus TCAD simulation tools .....	7
<b>Figure 1.6:</b> Floating-gate voltage dependence on the control-gate voltage for the UGFET device .....	9
<b>Figure 1.7:</b> Floating-gate voltage dependence on the charge density over the sensing area of UGFET device.....	9
<b>Figure 1.8:</b> Fabricated chip packaged in DIP 40 pin (a) with CMFET and UGFET devices and a snapshot (b) of an array of UGFET devices. ....	10
<b>Figure 1.9:</b> Snapshot of the fabricated chip showing single and an array of UGFET devices with bit and word lines for easy readout. ....	11
<b>Figure 1.10:</b> UGFET I-V measurements under dry conditions: with varying drain voltages .....	12
<b>Figure 1.11:</b> UGFET I-V measurements under dry conditions: drain current with varying control-gate voltages.....	12
<b>Figure 1.12:</b> UGFET I-V and transconductance curves with DI water, 0.01% poly Histidine, poly aspartic acid and 0.5% poly glutamic acid solutions.....	14

<b>Figure 1.13:</b> Subthreshold I-V curves tested for different concentrations of poly acrylic acid (PAA). .....	15
<b>Figure 1.14:</b> Relative voltage shifts with polyelectrolyte concentrations. ....	16
<b>Figure 2.1:</b> Examples of different nematode species.....	20
<b>Figure 2.2:</b> Microfluidic chamber and larvae. ....	23
<b>Figure 2.3:</b> The soft lithography steps used in the microfluidic channel fabrication.....	23
<b>Figure 2.4:</b> Measurement of locomotion parameters. (a): velocity (V), amplitude (A) and wavelength ( $\lambda$ ) from recorded videos. (b): oscillation frequency .....	26
<b>Figure 2.5:</b> Statistical distribution of the measured amplitude for SENS and LEVR <i>O. dentatum</i> larvae. ....	29
<b>Figure 2.6:</b> Measured wavelength for SENS and LEVR <i>O. dentatum</i> larvae without any drug exposure, SENS and LEVR <i>O. dentatum</i> larvae exposed to 1 $\mu$ M levamisole, and <i>H. glycines</i> SCN nematodes.....	30
<b>Figure 2.7:</b> (a) The tangential force $F_T$ exerted by each segment of the nematode's body results in the characteristic sinusoidal movement. (b) The amplitude to wavelength ratio for SENS and LEVR larvae without any drug exposure, SENS and LEVR larvae exposed to 1 $\mu$ M levamisole, and <i>H. glycines</i> SCN nematodes.....	32
<b>Figure 2.8:</b> Velocity measurements for SENS (dotted) and LEVR (solid) <i>O. dentatum</i> with and without exposure to levamisole.....	36
<b>Figure 2.9:</b> Video processing and extraction of motility parameters using an image-tracking program.....	38

<b>Figure 2.10:</b> Individual worm tracks of <i>O. dentatum</i> nematodes obtained from the image-tracking program.....	39
<b>Figure 2.11:</b> Distinct changes in the locomotion patterns of <i>O. dentatum</i> larvae in the microfluidic device at higher concentrations of levamisole .....	42
<b>Figure 3.1:</b> Fixed sine-wave channels: .....	47
<b>Figure 3.2:</b> Snapshots of a single nematode confined in sine-wave channel of fixed amplitude and changing wavelengths. ....	47
<b>Figure 3.3:</b> High throughput chip with sinusoidal wave channel. ....	49
<b>Figure 3.4:</b> Microphotographs of fabricated sine-wave channels in an experiment. ....	51
<b>Figure 3.5:</b> Velocity plots of the two different isolates of <i>O. dentatum</i> nematodes (SENS and LEVR) in fixed sine-wave channels with 120 $\mu\text{m}$ amplitude.....	54
<b>Figure 3.6:</b> Velocity plots for the LEVR isolate in sine-wave channels. ....	56
<b>Figure 3.7:</b> Velocity plots for the SENS isolate in sine-wave channels.....	56
<b>Figure 3.8:</b> Amplitude modulation and frequency modulation channels.....	58
<b>Figure 3.9:</b> Fabricated FM sine-wave channels.....	60
<b>Figure 3.10:</b> The average instantaneous velocity with respect to the wavelength is shown for SENS and LEVR <i>O. dentatum</i> larvae.....	62
<b>Figure 3.11:</b> The measured turning probability with respect to the wavelength for SENS and LEVR <i>O. dentatum</i> larvae.....	63
<b>Figure 3.12:</b> The measured stopping probability with respect to the wavelength for SENS and LEVR <i>O. dentatum</i> larvae.....	64
<b>Figure 3.13:</b> The cut-off region of the wavelength is shown for SENS and LEVR <i>O. dentatum</i> larvae. ....	65



<b>Figure 3.14:</b> Amplitude modulated sinusoidal wave channels. ....	67
<b>Figure 3.15:</b> The measured average instantaneous velocity with respect to the amplitude for SENS and LEVR <i>O. dentatum</i> larvae.....	68
<b>Figure 3.16:</b> The measured turn probability with respect to the amplitude for <i>O. dentatum</i> SENS and LEVR larvae.....	69
<b>Figure 3.17:</b> The measured stop probability with respect to the amplitude for SENS and LEVR <i>O. dentatum</i> larvae. ....	70
<b>Figure 3.18:</b> The cut-off region in AM device for SENS and LEVR <i>O. dentatum</i> larvae....	71
<b>Figure A1.1:</b> Sample graphic user interface for the image tracking software. ....	81
<b>Figure A1.2:</b> Screenshot of a running video data analysis. ....	82
<b>Figure A1.3:</b> Three processing steps of the raw video.....	84
<b>Figure A2.1:</b> Snapshots of the fixed sinusoidal channels.....	88
<b>Figure A2.2:</b> Snapshots of the amplitude modulated sinusoidal wave channels.....	88
<b>Figure A2.3:</b> Snapshot of the wavelength modulated sinusoidal wave channels.....	89

## Abstract

The idea of having an entire biological assay system on a single silicon wafer is promising with significant advantages in improving experimental throughput and sensitivity. This thesis presents three unique biological assays combining microfluidics and microelectronics technologies for high-throughput screening of biological samples: electronic sensors for detecting biomolecular charges, microchannels to characterize worm locomotion, and modulated trenches for differentiating mutant phenotypes.

The first chapter reports a novel floating-gate biosensor to detect and sense nano-scale charged particles such as charged poly amino acids. The device is fully CMOS compatible and has the ease of mass production. The new architecture of the floating gate enables scaling of the device area and incorporation of on-chip readout lines. Testing results show a strong sensitivity to the polarity and concentration of different poly amino acids tested. CMOS compatibility of the device is particularly useful while designing autonomous systems for biochemical sensing which require the on-chip integration of sensors, control circuitry, memory devices, and power lines.

The second chapter presents microfluidic bioassays for the phenotypic characterization of a certain class of animal and plant microorganisms called nematodes. Nematodes cause huge economic loss every year to agriculture and farm animals. In humans, exposure to meat or crops infected with nematodes cause long-term depression and reduced work productivity. However, with prolonged exposure to anthelmintic drugs, nematodes have evolved into new strains with varying levels of resistance to known drugs. With a goal to differentiate different isolates, the bioassay measures phenotype using parameters of

nematode locomotion. We characterize two different species of nematode and two isolates within one species: a plant parasite Soybean Cyst Nematode (SCN) and two isolates of an animal parasite *Oesophagostomum dentatum*. Parameters of sinusoidal motion such as propagation velocity, wavelength, wave amplitude, and oscillation frequency depend on the levamisole-sensitivity and strain of parasitic nematode. There are significant differences between the two strains (SENS and LEVR) and the two species (*O. dentatum* and SCN). This microfluidic technology advances present-day nematode migration assays and provides a better quantification and increased drug sensitivity. It is anticipated that the bioassay will facilitate study of resistance to other anthelmintic drugs that affect locomotion.

In the third chapter we report a new scheme to passively screen and sort different isolates of parasitic nematodes that may be visually indistinguishable. Unlike previous devices that immobilize worms or chemically treat them in micro scale chambers, we allow the nematodes to pass through modulated sinusoidal trenches and observe their locomotion at real-time. We then define and characterize locomotion parameters that help us identify and distinguish isolates automatically. We demonstrate this simple scheme of sorting whole animals using two isolates of *O. dentatum*. In addition, a custom image tracking software is developed to enable automated extraction and analysis of the experiments performed. Such bioassays are critical towards advancing high-throughput screening methods on whole organisms – a field that is relatively new in the scientific community.

## Chapter 1

# Scalable, CMOS-compatible Floating-gate FET for Detection of Charged Biochemical Molecules

## 1.1 Introduction

In recent years, there has been significant advances in the area of non-invasive, portable sensors that would couple chemical and biological entities with semiconductor devices and integrated circuits [1-5]. These include electronic sensors for the detection of chemicals, DNA hybridization, enzyme reactions, action potentials and protein complexes. To address the issues of post-processing, label-free detection and bulky instrumentation in traditional electrochemical sensors [2-6], a CMOS-compatible extended floating-gate field-effect transistor (EGFET) device was demonstrated for the electronic detection of electrolytes [7] and DNA hybridization [8,9]. In these EGFETs, the floating-gate is capacitively coupled to the sensing area (where biochemical species are adsorbed) in one direction and to the control-gate (where the readout voltage is applied) in the other direction [7-9]. The threshold voltage is a function of the applied control-gate voltage and the charge on the sensing area. Fluctuations in the amount of biochemical charge are electronically detected by a corresponding shift in the threshold voltage. However, with the present floating-gate topology of EGFETs, the sensing area is large ( $40\ \mu\text{m} \times 40\ \mu\text{m}$  to  $100\ \mu\text{m} \times 100\ \mu\text{m}$ ) [6] and device scalability is a challenge. Furthermore, a large sensing area lowers the device sensitivity to charge fluctuations [7]. As a solution, non-planar EGFETs have been proposed to shrink the sensing area by combining MEMS micromachining and CMOS fabrication steps [4]. In this chapter, we review two classical microelectronic chemical

sensors and demonstrate a new architecture for an EGFET device. Compared to previous EGFET designs [7-9], the floating-gate now spans the entire device. This allows us to significantly scale the total device area without compromising the amount of biochemical charge being sensed.

### **1.1.1 Ion Selective FET**

The first pioneering work on biosensors based on Ion-selective field effective transistor (ISFET) was reported in 1972 [10]. The ISFET is primarily a MOS field-effective transistor with a gate used as a reference electrode. This gate electrode is exposed in an aqueous solution, as illustrated in Figure 1.1. The voltage induced on the gate electrode is modified by the nature (pH, ionic concentration) of the solution. This gate voltage is monitored by measuring the current flowing between the ISFET's drain and source terminal.

During the past three decades, considerable work has been reported on improving the ISFET sensitivity, noise cancellation techniques, and sensor integration on-chip. Compatibility with standard CMOS fabrication process and the need for an additional reference electrode has been challenging issues for the scientific community. Additional post-processing steps such as coating with dielectrics are required to properly insulate the ISFET from the exposed chemical solutions. This limits the commercial worth of ISFET devices compared to other electronic devices such as microprocessors and flash memories.

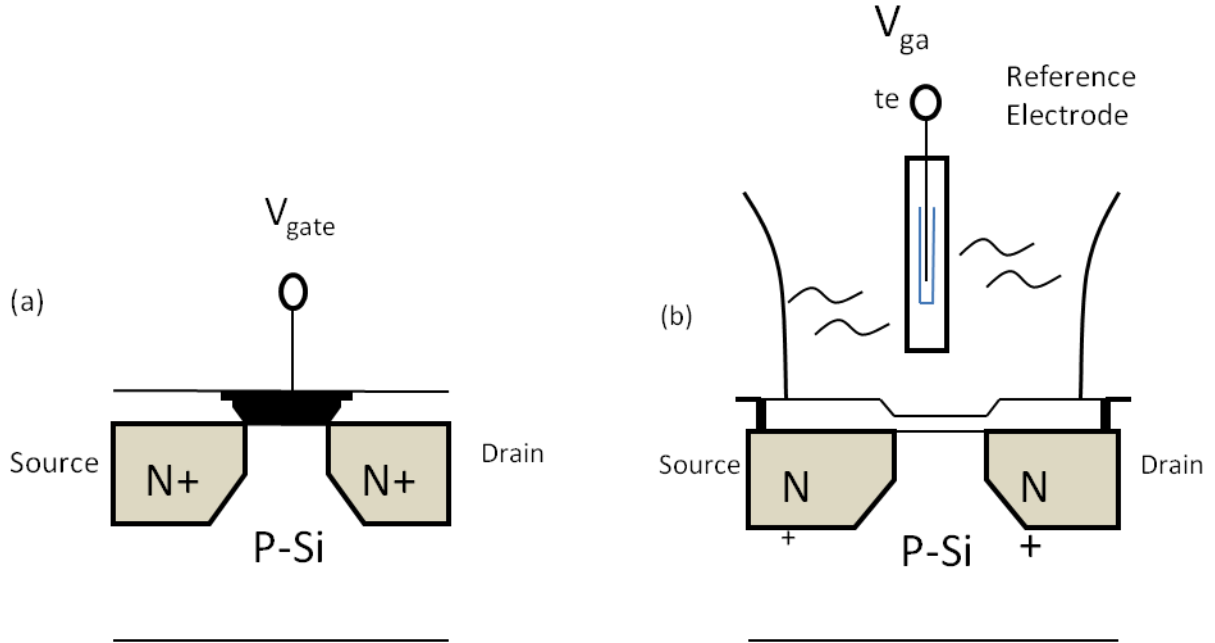


**Figure 1.1:** Schematic views of a MOSFET (a) and ISFET (b).

### 1.1.2 Chemoreceptive Neuron MOS

A group of researchers at Cornell University reported a modified version of a CMOS transistor for biosensing, which they named extended floating gate transistor (EGFET) [11, 12]. In this structure, the CMOS device has a floating gate that is capacitively coupled to the control gate on one side and sensing gate on the other side. Control gate induces voltage on the floating gate, turning on the transistor channel, while charges on the sensing gate modifies the floating gate voltage, and result in a shift in drain current. Change of floating gate voltage is directly related to the control gate voltage and the amount of charge on the sensing gate. However, as seen in Figure 1.2, this device requires a large area to isolate the extended control gate and sensing gate. This prevents device miniaturization and integration with VLSI components. Additionally, the device operation requires a large voltage (30V) for tunneling electrons into and out of the floating gate.

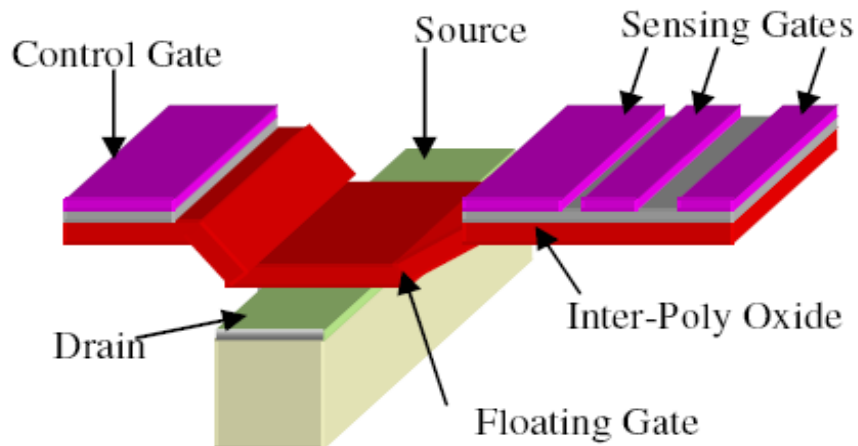


**Figure 1.2:** Illustration of a CvMOS transistor. Three-dimensional rendering of the device structure with potential multiple sensing gates [11].

## 1.2 Proposed Umbrella-Shaped Field Effect Transistor (UGFET)

We present a new architecture for extended floating-gate FET where the floating-gate spans the entire device area. We call it an Umbrella-shaped Floating-Gate (UGFET). The device comprises a FET with a control-gate, a floating-gate and a sensing area. The proposed UGFET is a combination of neuron FET-based sensor, chemicapacitors and a novel floating-gate structure. This allows us to significantly scale the total device area without compromising the amount of biochemical charge being sensed. Compared to the previous EGFET design, this work drastically reduces the chip area (from  $100\ \mu\text{m} \times 100\ \mu\text{m}$  to  $14.4\ \mu\text{m} \times 28.4\ \mu\text{m}$ ). A scheme for parallel readout of multiple devices in an array is shown. The chip is biocompatible and allows growth of neuronal cultures without detrimental effects on the bio-FETs. This would enable possible real-time, non-invasive observation of biologically relevant growth and adaptability processes of cells with applications to several neurodegenerative diseases.

### 1.3 UGFET Design and Analysis

As shown in Figure 1.3, the device comprises a floating-gate that is capacitively coupled to a control gate (CG) and connected to a sensing area (SA). The floating-gate covers the entire device to maximize the sensing area and minimize the lateral dimensions. The biochemical solution is placed on the sensing area that is covered with overlay glass deposited during the last step of CMOS fabrication. The floating gate is capacitively coupled to this sensing area to electronically read out any charge fluctuations on the sensing area.

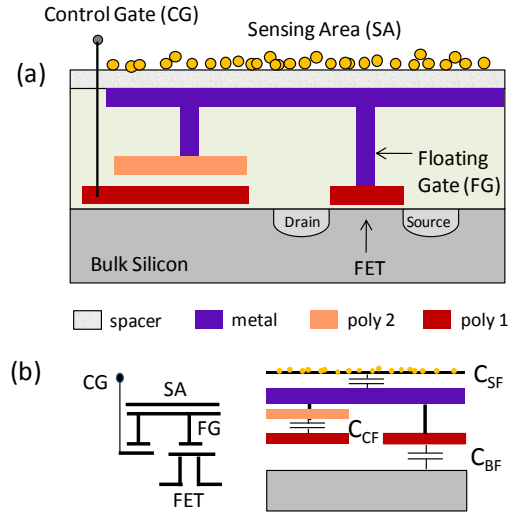


**Figure 1.3:** (a) Cross-section of the proposed UGFET and its symbolic representation with an equivalent capacitance model (b).

The induced voltage  $V_{FG}$  on the floating-gate of bio-FET shown in Figure 1.3 is written as:

$$V_{FG} = \frac{C_{CF}}{C_T} V_{CG} + \frac{Q_{F0} + Q_i}{C_T} = \frac{C_{CF}}{C_{SF} + C_{BF} + C_{CF}} V_{CG} + \frac{Q_{F0} + Q_i}{C_{SF} + C_{BF} + C_{CF}} \quad \text{Equation (1.1)}$$

where  $C_{CF}$  represents capacitance between control-gate and floating-gate,  $C_{SF}$  is the capacitance between sensing area and floating-gate,  $C_{BF}$  is the capacitance between floating-gate and the bulk,  $C_T$  is the total capacitance of the device [5],  $V_{CG}$  is the applied voltage on



the control-gate,  $Q_{F0}$  is the static charge on floating-gate and  $Q_i$  is the total induced charge on sensing area. In our experiments,  $Q_{F0}$  is taken as the ‘reference’ charge on the floating-gate with deionized (DI) water on the sensing area. Addition of charged biomolecules alters the voltage on the floating-gate [7-9]. Positively charged molecules increase  $V_{FG}$  and thus a smaller  $V_{CG}$  is required to turn on the device. This produces a lower threshold voltage ( $V_T$ ) and a negative shift in the current-voltage (I-V) curve compared to that for DI water. Alternatively, negatively charged molecules lower the floating-gate voltage  $V_{FG}$  and require a higher control-gate voltage  $V_{CG}$  to turn on the device.

We designed the UGFET sensor using SCMOS rule in Cadence and fabricated by AMIS 1.6  $\mu\text{m}$  technology. The sensing gate is  $14.4 \mu\text{m} \times 28.4 \mu\text{m}$ . Since the floating-gate is totally isolated, its total charge remains a constant. This charge conservation principle was used earlier to arrive at Equation (1). The UGFET’s effective threshold voltage depends on the amount and nature of surface charges over the sensing area. Positive surface charges  $Q_s$  cause a negative shift in the effective threshold voltage, while negative surface charges  $Q_s$  give a positive shift in the threshold voltage (for n-channel UGFETs and vice versa for p-channel UGFETs).

Using the initial 1-D modeling, a 3-D UGFET device model is constructed using Synopsys® Sentaurus Structure Editor. This helps create a realistic device structure according to the AMIS technology profile used later for device fabrication. The design is built using Scalable CMOS (SCMOS) design rules available through Cadence. The semiconductor parameters such as doping density, the oxide thickness, the metal thickness *et al* are extracted from the test data available on MOSIS website ([www.mosis.com](http://www.mosis.com)) for AMI

1.5  $\mu\text{m}$  technology. By the simulation, we are able to visualize the charge redistribution and potential profile due to the charge fluctuations over the sensing area. A snapshot of the UGFET structure is shown in Figure 1.4. Figure 1.5 shows a snapshot of the three dimensional electrical potential distribution of the UGFET. The developed 3-D device model takes into account all parasitics such as fringe capacitance and overlap capacitance. The 3-D capacitance values appear to be approximately 9-12% deviated from those obtained using a 1-D model. As expected, compared to a 1-D model, the 3-D model gives a better representation of the device physics and electric field profiles as the device structure is scaled down.

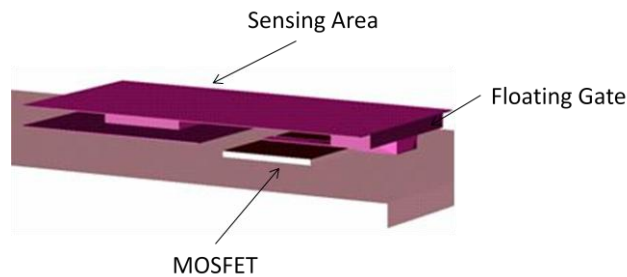


**Figure 1.4:** Three-dimensional UGFET cross-section built with the Synopsis device simulator.

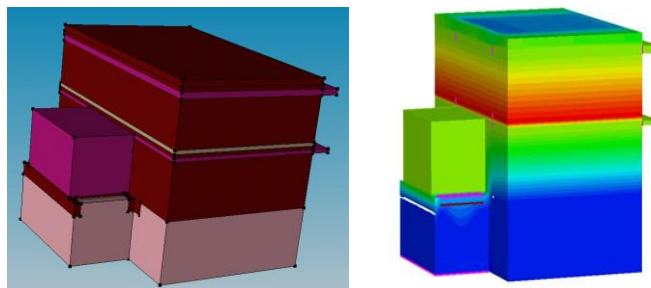
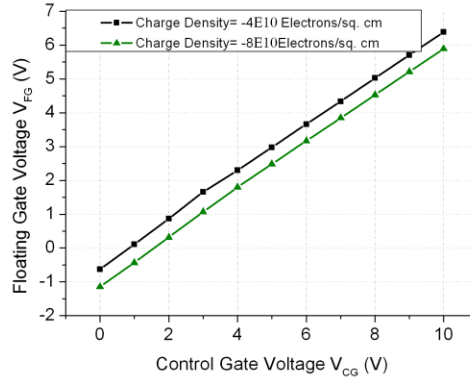


**Figure 1.5:** Three-dimensional electrical potential distribution of UGFET using Sentaurus TCAD simulation tools

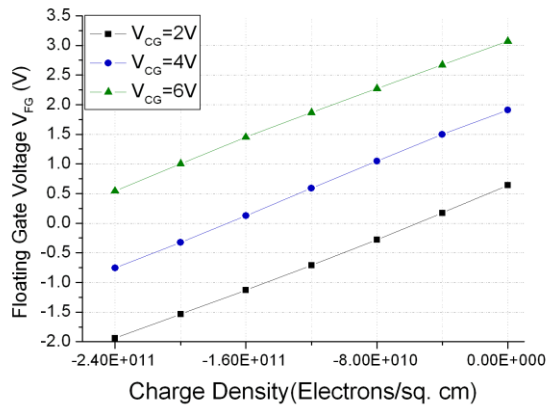
Extensive simulation studies were performed to scale the device dimensions without sacrificing the sensitivity. Two important results are shown here. In Figure 1.6, the control-gate voltage is varied from 0V to 10V. Two cases are plotted where the charge densities are  $4 \times 10^{10}$  electrons/cm<sup>2</sup> and  $8 \times 10^{10}$  electrons/cm<sup>2</sup>. The spacer is 200 nm thick and separates the floating gate from external charges. A linear relationship is shown between the floating gate voltage and control gate voltage as derived in Equation (1.1).

Figure 1.7 shows the dependence of floating-gate voltage on the charge density placed on the sensing area. The spacer thickness is chosen as 30 nm. Three cases are plotted for three different control-gate voltages: 2V, 4V and 6V. We observe a linear relationship between the floating-gate voltage and charge density to be sensed. This again follows from Equation (1.1). The floating-gate voltage also depends on spacer thickness. A thicker spacer induces less potential on floating-gate but this dependence is negligible.

During an experiment, the amount of charge (e.g. from single stranded DNA) immobilized on the sensing area can be easily modified and this, in turn, modulates the UGFET's threshold voltage [5]. The shift in threshold voltage is usually determined by measuring the drain current at a constant control-gate voltage or by measuring the control-gate voltage at a constant drain current. The electronics instrumentation can also be programmed to repeat the device measurements over a period of time. This would help detect and monitor any subtle charge fluctuations due to some chemical reactions over the sensing area (e.g. DNA hybridization, antigen-antibody interactions, cell migration, stem-cell differentiation, synaptic transmission, or inter-neuron communication) [8].



**Figure 1.6:** Floating-gate voltage is linearly dependent on the control-gate voltage for the UGFET device as observed from the device simulations. The two plots are from two values of charge densities on the sensing area.



**Figure 1.7:** Simulation results show the floating-gate voltage is linearly dependent on the charge density over the sensing area of UGFET device. The three plots are related to three values of the control-gate voltage.

#### 1.4 UGFET Fabrication

We designed the sensor using SCMOS rule in Cadence Virtuoso. UGFET devices are fabricated through a commercial foundry (MOSIS AMIS 1.6  $\mu\text{m}$  technology). This process technology has a feature size of 1.6  $\mu\text{m}$ , which means the minimum gate length of the MOSFET is 1.6  $\mu\text{m}$ . This technology has two poly-silicon layers (poly 1 and poly 2) and two

metal layers (aluminum) for electrical interconnects. The capacitance between poly1 and poly2 layer is large and is used to create the capacitive coupling between the control gate the floating gate. Devices (CMFETs and UGFETs) with various dimensions ( $14.4 \mu\text{m} \times 28.4 \mu\text{m}$  to  $100 \mu\text{m} \times 100 \mu\text{m}$ ) are included in one single chip and packaged in DIP40. Figure 1.8 shows the packaged chip along with a snapshot of the devices on the chip [13].

The transistor designs are relatively scaled based on the device width/length ratio of  $4.5 \mu\text{m} / 1.5 \mu\text{m}$ . The gate oxide thickness is 30 nm and the devices are fabricated in p type silicon substrate. The threshold voltage average for regular NMOS transistors is 0.56V in this run. No post fabrication process is performed for the devices.

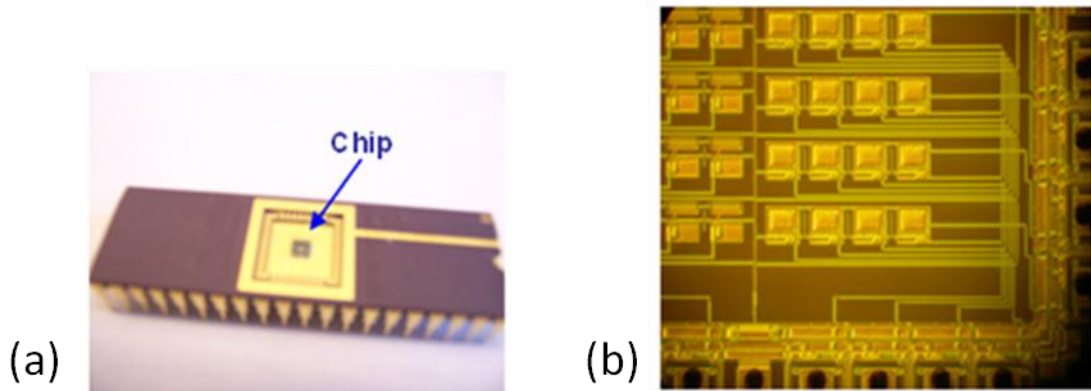


**Figure 1.8:** Fabricated chip packaged in DIP 40 pin (a) with CMFET and UGFET devices and a snapshot (b) of an array of UGFET devices.

## 1.5 Experimental Results

The performance for any sensors is characterized by testing its sensitivity, stability, and reproducibility. Our UGFET devices, as shown in Figure 1.8, are tested for these three benchmarks. Their performance is reported here. A high degree of consistency and reproducibility in the measured data are found during device testing. The semiconductor

parameter analyzer HP4155 is employed and custom LabVIEW™ programs are written for automated data-acquisition and controls of the various electronic instruments (HP4155, probe station and computer). In addition, an 8 x 8 array of the smallest devices ( $14.4 \mu\text{m} \times 28.4 \mu\text{m}$ ) are fabricated. Similar to flash memory cells [6], bit and word lines are included for parallel readout of multiple devices in the array, as shown in Figure 1.9.

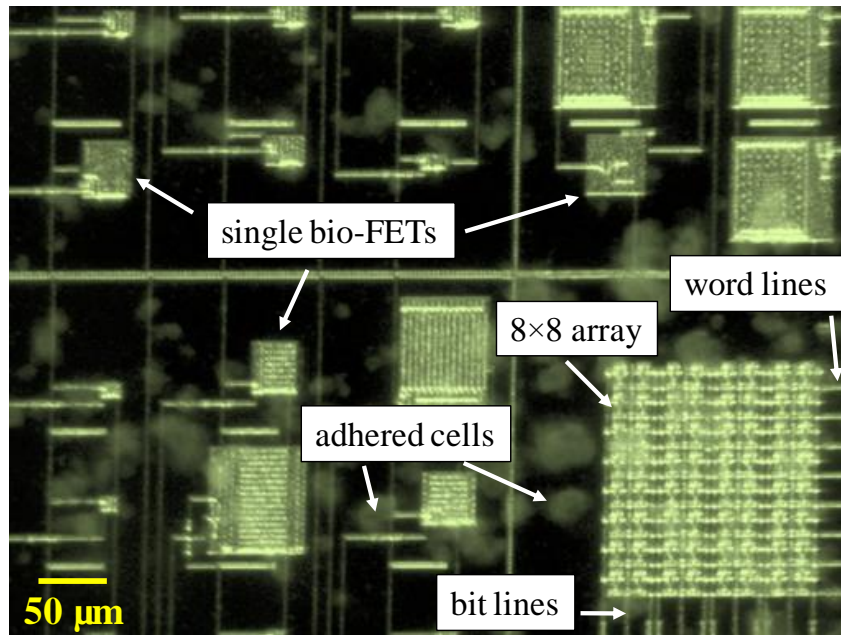


**Figure 1.9:** Snapshot of the fabricated chip showing single and an array of UGFET devices with bit and word lines for easy readout. Cell lines placed on the chip adhered and are growing into neurons (translucent globules).

### 1.5.1 Electrical Characterization

The fabricated UGFET devices are tested under dry conditions and drain to source current measurements are performed, as shown in Figure 1.10. Judging from the characteristics of the plots in Figure 1.10, we confirm that the fabricated UGFET devices work well as extended floating-gate field-effect transistors. The voltage applied to the control-gate is able to induce a potential change on the floating-gate and turn the device ‘on’

[6]. The sensitivity of the floating-gate potential on the control-gate voltage follows from the simulation results shown earlier in Figure 1.6 [13].

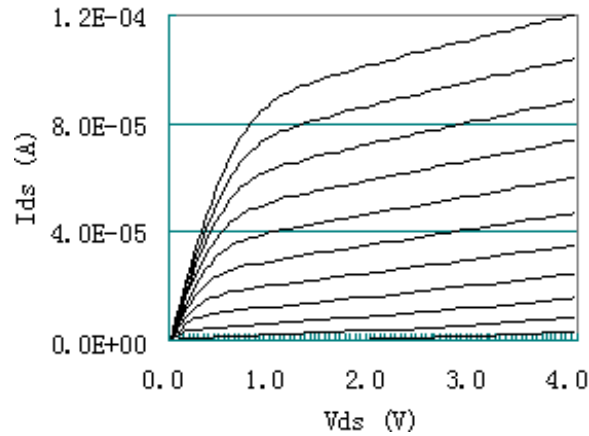


**Figure 1.10:** UGFET I-V measurements under dry conditions: with varying drain voltages

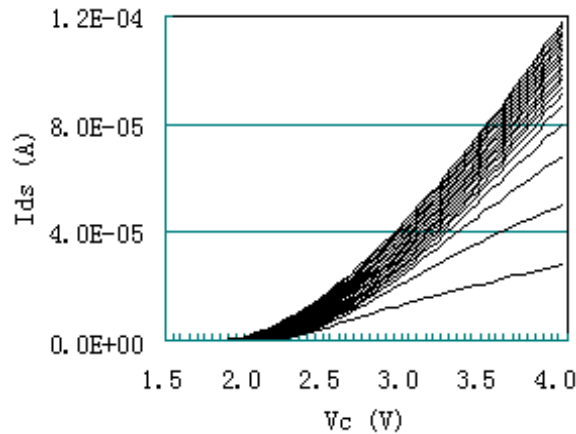


**Figure 1.11:** UGFET  $I_{ds}$ - $V_c$  (control gate voltage) measurements under dry conditions: drain current with varying control-gate voltages

### 1.5.2 Transconductance Measurement

The UGFET device is tested for its charge-sensing ability with a small volume of the following charged poly amino acid: 0.01% poly histidine, 0.5% poly glutamic acid, and 0.5% poly aspartic acid, as shown in Figure 1.12. The control gate voltage is swept from 0V to

4V while keeping the drain voltage fixed at 0.4V. The drain currents are recorded. The transconductance curves are shown in Figure 1.12 [14]. As observed from Figure 1.12, positively charged poly histidine produces a negative threshold voltage shift ( $\sim 0.1V$ ), while negatively charged poly glutamic acid and poly aspartic acid produce a positive shift of  $\sim 1.2V$  and  $\sim 0.35V$  respectively. The relative shifts in the threshold voltage can be explained as follows: poly histidine, similar to poly-L-lysine, is a positively charged amino acid solution and its polycationic nature is known to attract the anionic groups of a biological sample and promote adhesion. Since surface charges  $Q_S$  on the sensing area are positive, threshold voltage is reduced due to a larger floating-gate voltage under the same control-gate voltage. The drain current curve is hence shifted left of the DI water reference curve. The smaller shift for poly histidine is attributed to its very low concentration. Negatively charged poly aspartic acid and poly glutamic acid shift the  $g_m-V_{CG}$  curves to right of DI water reference. The higher concentrations of other poly amino acids translate to larger threshold voltage shifts, as shown in Figure 1.12. All measurements are repeated several times and the data are consistent. The chip is reusable and rinsing with DI water is sufficient to restore the reference I-V curve.



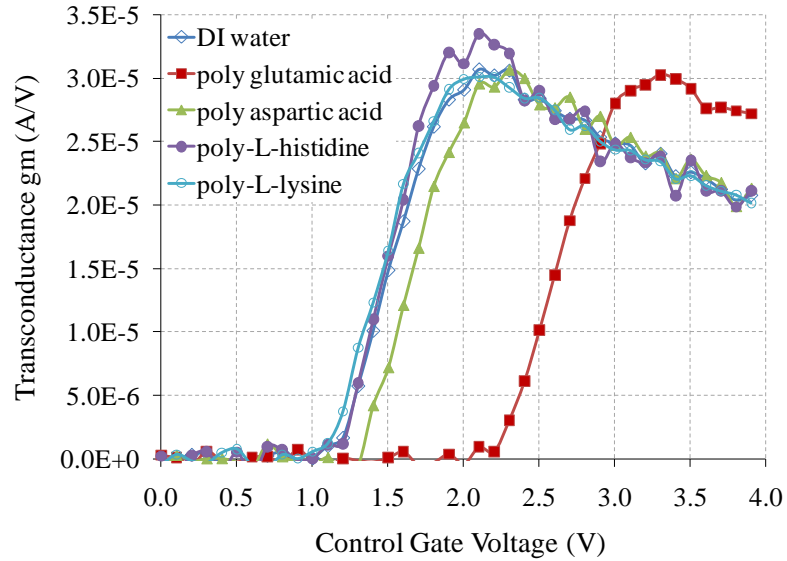


**Figure 1.12:** UGFET I-V and transconductance curves tested with DI water, 0.01% poly Histidine, 0.5% poly aspartic acid and 0.5% poly glutamic acid solutions.

The threshold voltages are extracted from Figure 1.12 using the transconductance method [7]. For the case of DI water reference, the threshold voltage is 1.5V. A differential threshold voltage ( $\Delta V_T = V_{T\_poly} - V_{T\_DI}$ ) is calculated for each poly amino acid. For positively charged poly-L-histidine and poly-L-lysine, the  $\Delta V_T$  values are -0.1V and -0.08V respectively. The  $\Delta V_T$  values for negatively charged poly aspartic acid and poly glutamic acid are 0.35V and 1.2V respectively. Both poly-L-histidine and poly-L-lysine have a much lower (0.01% w/v) concentration which explains their smaller  $\Delta V_T$  magnitude. Poly aspartic acid and poly glutamic acid are at a higher (0.5% w/v) concentration and hence produce a larger  $\Delta V_T$  magnitude. Each I-V measurement is done 5-8 times and repeated (5-8 times) after refreshing the device using the above mentioned steps (Section II). The  $\Delta V_T$  values are consistent which indicate reliability in detecting biochemical charges using the bio-FETs.

### 1.5.3 Subthreshold Measurement

We also measure the subthreshold characteristics of the devices [15]. In subthreshold region, the I-V curve follows an exponential relationship, as given in Equation (1.2).  $I_0$  and  $n$  in the Equation (1.2) are constants related to the size and doping of the device.

$$I_D = I_0 \exp\left(\frac{V_{CG} - V_{TH}}{nV_T}\right) \quad \text{Equation (1.2)}$$

The control-gate voltage is fixed at 2.5V and the drain voltage is swept from 0V to 2V. The subthreshold I-V curves are recorded for different concentrations of PAA solution, as shown in Figure 1.13. The devices are refreshed after each run of 5-8 trials and reused. The subthreshold I-V curves show a consistent shift to the left with increasing PAA concentration [16]. A higher concentration of PAA molecules increases the surface potential and lowers the threshold voltage  $V_T$ . The subthreshold slope  $S$  is unaltered, indicating that the charge distribution is undisturbed during individual experiments [7]. These results are also expected from our simulations.

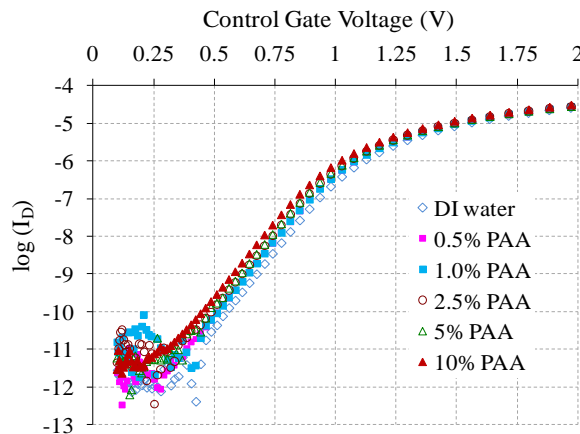


**Figure 1.13:** Subthreshold I-V curves tested for different concentrations of poly acrylic acid (PAA).

To show concentration-dependent change in the threshold voltage, three other poly amino acids (PSASS, PAHC and PDDAC) are tested as shown in Figure 1.14). The differential threshold voltage increases with increasing concentration of the charged poly amino acids.

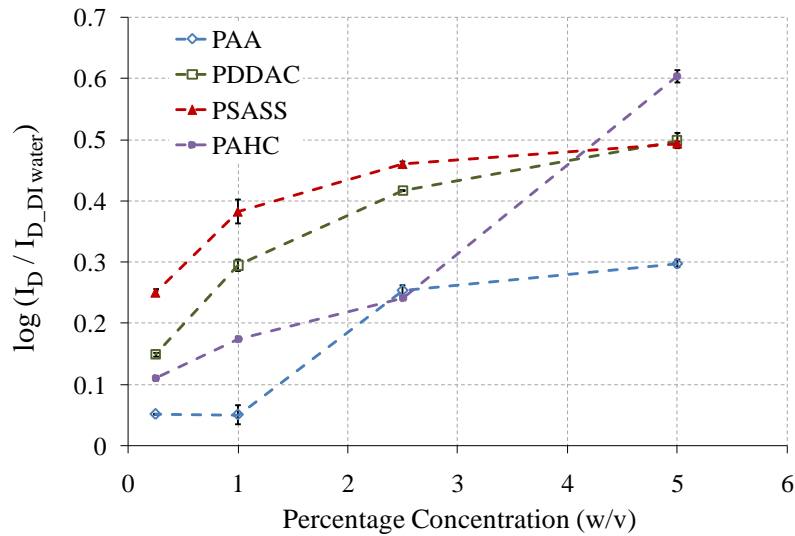


**Figure 1.14:** Differential threshold voltages (difference in a device's threshold voltage with poly amino acid and with DI water) values versus percentage concentration of four poly amino acids (PAA, PDDAC, PSASS and PAHC).

To demonstrate feasibility of the UGFETs for VLSI integration, we fabricated an 8×8 array of the smallest (14.4 μm×28.4 μm) devices. The control-gates of a single row are connected to form a bit line while drain electrodes of a single column are connected to form a word line. Each of the eight bit and word lines are addressable by an external analog-digital converter and a LabVIEW™ program. I-V characteristics of individual bio-FETs in the array are similar to those isolated devices, as shown in Figure 1.10 and Figure 1.11. Fabrication in another technology node (possibly 0.18 μm or 40 nm) will enable further scaling of the array.

One possible application of a high density array of bio-FETs is the real-time monitoring of neuronal growth and cell-cell communication. To demonstrate on-chip cell growth and viability, neuronal cell lines (suspended in standard cell culture media) are dropped on the fabricated chip which then adhere to the chip surface and grow over time. The snapshot in Figure 1.9 shows successful adherence and growth of neurons on the chip surface three days after placing the cell lines. I-V characteristics of the devices are stable through the three days of neuronal growth. This suggests good physical and chemical isolation of the floating gate and minimal penetration of ions in the culture media through the overlay glass.

## 1.6 Discussion

The basic operation principle of UGFETs is similar to signal conduction mechanisms in neurons and synaptic clefts. The UGFET can be viewed as having multiple control-gate electrodes, each capacitively coupled to the extended floating-gate. The voltage induced on the floating gate is a weighted sum of the voltages applied to the control-gate electrodes. In our case, there are two ‘controls’ contributing to the floating-gate potential: the control electrode and the biomolecular charges over the sensing area.

Since UGFET charge-sensing mechanisms discussed here are purely capacitive, the control-gate voltage can be scaled down and easily integrated with other on-chip VLSI components. This is particularly useful in designing autonomous systems for biochemical sensing which require the on-chip integration of sensors, control circuitry, memory devices, and power lines. This was a disadvantage for previous CMFET and neuromorphic FET sensors that rely on tunneling-based mechanisms and therefore need higher operating voltages [6]. No special post-processing (e.g. glass cut [5] or nitride passivation [6]) is

required for our UGFET devices. Furthermore, the UGFET has a reduced device area which leads to better charge sensitivity and possible large-array applications.

In summary, our work has presented a novel charge-sensing platform using an extended floating-gate device (UGFET) that is scalable and fully compatible with standard CMOS process. Simulation results predict a very high sensitivity compared of previous neuron FETs: 150 pico Coulombs of charge per  $\text{mm}^2$  on the sensing area produces  $\sim 1\text{V}$  change in the floating-gate. The fabricated sensor arrays are tested as charge-modulated biochemical sensors. This neuromorphic sensing method is nondestructive, repeatable, reusable, and easily refreshed. The transconductance and subthreshold measurements verified that the UGFETs show markedly different responses between polyelectrolyte and poly amino acids of varying polarity and concentration. Since most biological species (single cells, proteins, DNA) have intrinsic charge, UGFET charge-modulated microarrays could serve as fast, portable, and inexpensive alternatives for biochemical sensing applications. Additionally, the chip is biocompatible and allows growth of neuronal cultures without detrimental effects on the UGFETs. This would enable possible real-time, non-invasive observation of biologically relevant growth and adaptability processes of cells with applications to several neurodegenerative diseases.

## Chapter 2

### **MEMS Bioassay for Characterizing Nematode Phenotype**

#### **2.1 Introduction**

Nematode parasites cause disease in plants, animals and humans causing economic loss to agricultural and food industry. The control of plant parasitic nematodes has involved crop rotation, biological control and use of chemicals. In animals and humans, where there is an absence of vaccines, and sanitation is poor, control of these infections has relied on regular chemotherapy. Drug resistance has emerged in parasites of animals [17] and humans [18]. Early detection of drug resistance is necessary for limiting its spread. Although some molecular methods are available for detecting a changed genotype associated with resistance [19, 20] detection of resistance in nematode parasites is mainly based on detecting a changed phenotype. Many classes of anthelmintics (haloxon, levamisole, monepantel, derquantel, ivermectin and piperazine) act on the neuromuscular system of nematodes to inhibit locomotion [21, 22]. It is likely that drug resistance will be associated with a change in the phenotype of locomotion as signaling pathways are modified. Figure 2.1 shows several examples of nematodes along with crops infected by nematodes.

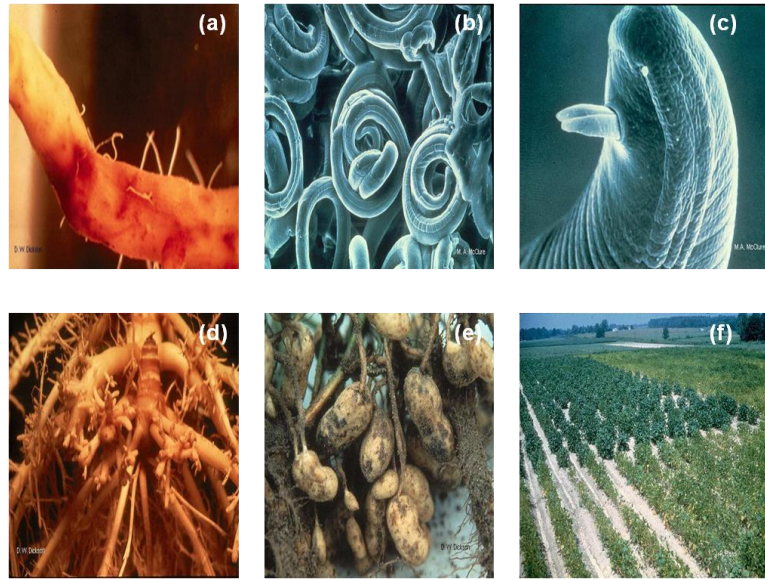


**Figure 2.1:** Examples of different nematode species: *Hoplolaimus galeatus* (a), *Aphelenchus avenae* (b), and *Meloidogyne incognita* (c). Various species of nematodes infect different crops-- (d) corn roots damaged by *Paratrichodorus minor*, (e) Peanut pods damaged by *Pratylenchus brachyurus*, and (f) resistant and susceptible soybean growing in a *Heterodera glycines* infested field are shown. (Pictures from <http://www.nematologist.com>)

Here, we describe a method for characterizing the movement phenotype of larvae of parasitic nematodes by quantitative measurement of their locomotion in microfluidic chambers. We show that phenotype varies with the species and strain of the tested nematodes. We show that the dose response measurement of the forward velocity is detectably different between resistant and sensitive strains of an animal parasitic nematode.

Most nematodes rely on side-to-side slithering movement to ‘swim’ over solid surfaces. Their mechanism of locomotion has intrigued researchers for several decades and inspired a number of quantitative models to explain the nature of undulatory motion [23, 24, 25, 26]. In the model nematode, *C. elegans*, locomotion experiments have often been performed on agar plates where the *C. elegans* uses the surface tension of thin surface water

film and its internal hydrostatic pressure to generate the forward motion force [27-29]. The oscillatory movement of the head is propagated backwards along the rest of the body as sinusoidal waves [25, 30]. Recently, microfluidics technology has enabled the fabrication of a new class of devices such as micro-chambers, mazes, wave sampler and cylindrical posts to study worm behavior in structured and challenging microenvironments [25, 31-34]. Amongst other benefits, microfluidics technology offers experimental resolution at the micro scale level, thereby allowing the experimentalist to observe, track, and characterize locomotion of a single worm over time [34]. On-chip immobilization of nematodes on microfluidic devices with high-resolution imaging of its neurons and other cellular activity has also generated great interest in the neuroscience community [31, 35-37].

In this work, we extend the application of microfluidics technology to the study of parasitic nematodes and demonstrate differences between species of nematode. More importantly, the approach can distinguish different isolates of the same species. We designed and fabricated microfluidic assays to record and characterize the undulatory movement of larvae of the pig parasite *Oesophagostomum dentatum* and the soybean cyst nematode (SCN), *Heterogena glycines*. Two isolates of the *O. dentatum* species were tested: levamisole-sensitive (SENS), which are sensitive to the cholinergic anthelmintic levamisole and levamisole-resistant (LEVR), which are resistant to the drug at therapeutic doses. The parameters under study were the velocity of forward migration, amplitude and wavelength of the sinusoidal motion, and the frequency of side-to-side slithering action of the nematodes. We observed clear differences between SENS and LEVR *O. dentatum* larvae allowing the drug resistant phenotype to be identified in the absence of the anthelmintic drugs. We



characterized the anthelmintic dose response for SENS and LEVR isolates and noticed differences in the degree of their drug resistance. We also observed distinct differences in locomotion parameters between larvae of *H. glycines* and *O. dentatum*.

## 2.2 Device Design and Analysis

### 2.2.1 Fabrication of Microfluidic Devices

The microfluidic devices were designed to have multiple straight, parallel channels (width = 300  $\mu\text{m}$ , length = 1 cm, height = 40  $\mu\text{m}$ ), each with its individual input and output ports. The device dimensions can be easily altered at the design stage to be adapted to a certain species of nematodes under test. The fabrication was done using standard micromachining and soft lithography procedures [33]. The mask layout was drawn in Adobe Illustrator and sent to an outside vendor (Photoplotstore, Colorado Springs, CO) to generate the masks. A 40  $\mu\text{m}$ -thick SU-8 photoresist (Microchem Corporation, Newton, MA) was cast on a bare silicon wafer by spin coating (~1000 r.p.m.). Standard photolithography was carried out to create the final SU-8 master mold. The PDMS prepolymer (Sylgard-184 Silicone Elastomer Kit, Dow Corning Corporation, Midland, MI) was cast over the SU-8 mold and cured on a hot plate at 70°C for two hours. Subsequently, the PDMS microfluidic devices were peeled off the mold and input/output ports (2mm diameter) were created using a sharp needle. Air plasma was exposed to the PDMS devices, which are then bonded to individual glass cover slips. The mask is shown in Figure 2.2 (a). The pictures of two species of nematodes used in our experiments are shown in Figure 2.2 (b), which is *O. dentatum* (left) and *H. glycines* (right). Figure 2.3 shows a block diagram of the soft lithography steps discussed above.

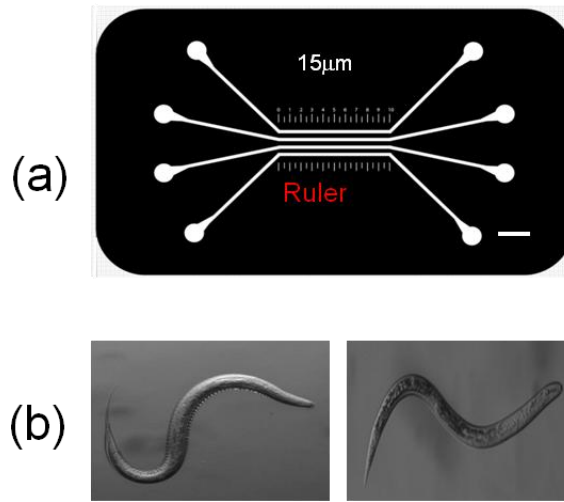


**Figure 2.2:** Microfluidic chamber and larvae. (a): the mask for the four-channel microfluidic device to study nematode locomotion. There are vertical markers to help calibrate the forward velocity. (b): pictures of the organisms used in our experiments: *O. dentatum* (left) and *H. glycines* (right).

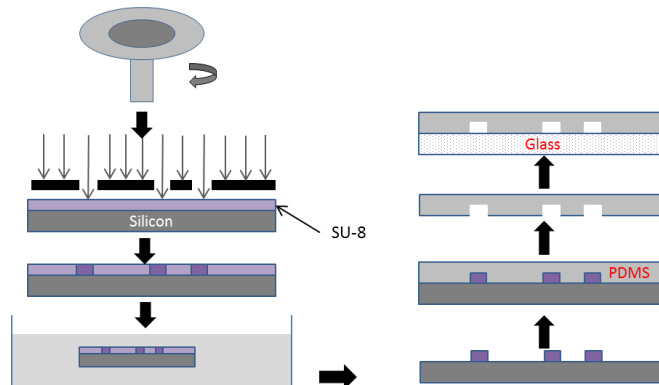


**Figure 2.3:** The soft lithography steps used in the microfluidic channel fabrication.

### 2.2.2 Sample and Medium Preparation

A 0.8 % agar (Fisher Scientific) gel in water was prepared. The mixture was put on a hot plate at 100°C and stirred for one hour. The molten agar was allowed to cool down to

37°C in a warm water bath. 0.36  $\mu\text{L}$  of agar was pipetted and filled in each of the four channels of the microfluidic device. Care was taken to ensure that input ports of the channels are not completely filled with agar or else, after a brief time (2 minutes), the excess gel-like agar was scooped and cleared out of the input ports. A small volume (1mL) of nematodes were pipetted and centrifuged to increase the concentration of the worms (100/ $\mu\text{L}$ ). The nematodes were then added to the agar and allowed to accommodate at 37°C for 10 minutes. Syringes were connected to the input ports of the microfluidic devices using rubber tubing. Subsequently, the agar gel mixed with nematodes was filled into the input ports of the four channels. After 5 to 15 minutes (the scouting time), the nematodes were seen entering the channels from the input ports and moving through the channel towards the output ports.

### 2.2.3 *O. dentatum* Larvae as Test Nematodes

*Oesophagostomum dentatum* were originally supplied by the Royal Veterinary and Agricultural School, Frederiksberg, Copenhagen and then reproduced at 6-9 month intervals by passage in pigs at Iowa State University, Ames, Iowa. The L3 larvae isolates were maintained between passages in tap water refrigerated at 11°C (changed every 2-4 months).

### 2.2.4 Data Capture and Analysis

The nematodes were observed with a Leica MZ16 transmission stereomicroscope using magnifications from 7.1x to 230x. A QICAM 12-bit Mono Fast 1394 Cooled digital camera interfaces with a QCapture Pro software for capturing individual digital images and digital image sequences. Digital image sequences of nematode movement were recorded at one-second time intervals with a resolution of 1392 x 1040 pixels and saved in uncompressed .avi video format. These videos were later imported into MATLAB where

individual frames are analyzed. An actual distance to pixel distance ratio was created by measuring the pixel width of a channel of known width using the MATLAB Image Toolbox. This ratio was used to translate pixel measurements to actual distance for the calculation of nematode velocity, amplitude and wavelength. The MATLAB Image Toolbox was used to measure pixel distance and was able to accommodate the angle and direction of nematode movement.

### 2.2.5 Calculation of Locomotion Parameters

Nematodes with unimpeded forward propagation exhibit a consistent velocity over distances much longer than their body length. Worm average velocity was defined as the continuous forward linear distance traveled by a worm's head with respect to time. In our experiments, average velocity over a length of the channel was measured by obtaining the total number of pixels traveled by the head of a nematode between a certain number of image frames (minimum 20) taken at one-second time intervals. The total number of pixels traversed between the beginning and the end frames was calculated using QCapture PRO software and translated to an actual distance using the previously mentioned ratio. This distance was then divided by the total number of frames between the beginning and end measurement positions to obtain an average velocity in  $\mu\text{m s}^{-1}$ .

Besides the average velocity, we measured parameters related to the sinusoidal body shape of nematodes during forward locomotion. As shown in Figure 2.4(a), the amplitude (A) was measured from latitudinal peak to peak, while wavelength ( $\lambda$ ) was measured from longitudinal peak to peak, as shown in Figure 2.4. The pixel distances of these attributes were measured using the MATLAB Image Toolbox. Pixel distance was converted to actual

distance in the units of micrometers using the previously mentioned ratio. The oscillation frequency was calculated as the reciprocal of the total time period needed for a given worm to return to its original state of sinusoidal pattern. A pictorial representation of the oscillation frequency is shown in Figure 2.4(b).

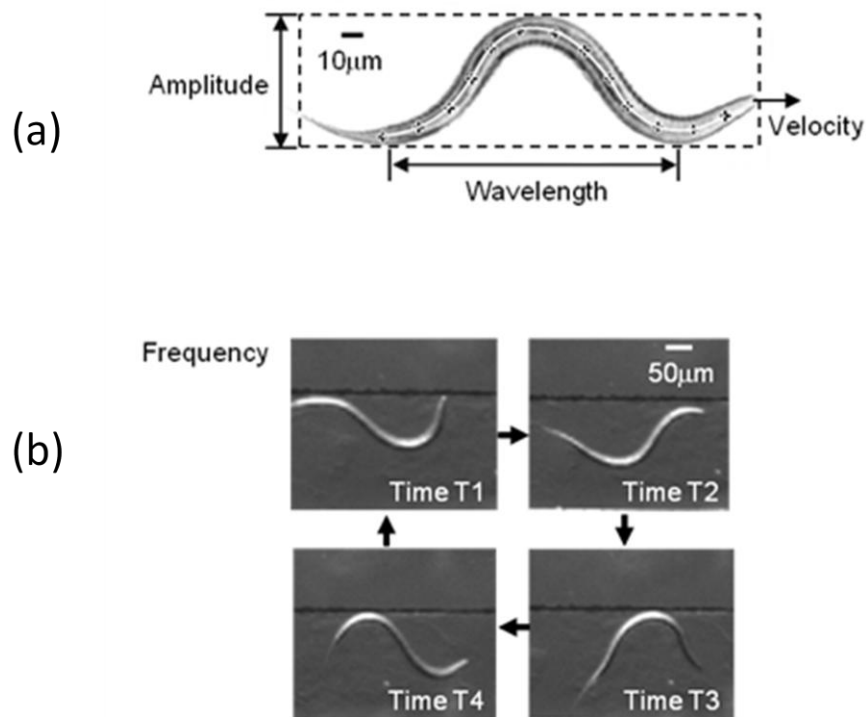


**Figure 2.4:** Measurement of locomotion parameters. (a): Illustrations of the SENS larvae for measurement of the velocity ( $V$ ), amplitude ( $A$ ), and wavelength ( $\lambda$ ) from the recorded videos. Individual images are separately analyzed from a video and a MATLAB<sup>®</sup> program is used to accurately measure the parameters with a resolution of  $0.1\mu\text{m}$ . (b): A fourth parameter, oscillation frequency, is calculated as the reciprocal of the total time period needed by a nematode to complete one sinusoidal wave motion. The figure shows a series of time-lapsed images of the same *H. glycines* as it moves along the agar-filled channel and the time period is 2 seconds (oscillation frequency =  $0.5\text{Hz}$ ).

These measurements of body parameters were only performed on worms that were normal to the viewing plane and clearly exhibit forward movement uninhibited by foreign

objects. We ignored image frame sequences where the worm under observation touched other worms, the sidewalls of the channel or any foreign particulates during its movement. This prevented distortion of their natural amplitudes and wavelengths and gave true information of their body parameters. Furthermore, care was taken to use a small and constant concentration of worms ( $\sim 100/\mu\text{L}$ ) in each channel so the chances of observing uninhibited forward movement of nematodes in the microfluidic device increase.

Unpaired t-tests were used to estimate statistical significance. Graph Pad V. 5.0 (GraphPad<sup>®</sup>, San Diego, C.A.) was used to carry out these tests.

## 2.3 Experimental Results

### 2.3.1 Amplitude Measurements

When we examined the amplitudes of the waves of contraction, we found differences between nematode isolates and species. Figure 2.5 shows examples of the amplitude observed with SENS and LEVR isolates of *O. dentatum*. Also shown are the distributions of SENS and LEVR amplitudes. SENS had an amplitude of  $135.2 \pm 1.7 \mu\text{m}$  (mean,  $\pm$  s. e.,  $n = 32$ ) which was significantly ( $p < 0.001$ ) larger than LEVR ( $122.5 \pm 1.8 \mu\text{m}$ , mean,  $\pm$  s. e.,  $n = 35$ ).

When we measured amplitude of the SENS and LEVR isolates in the presence of 1  $\mu\text{M}$  levamisole, we found that there was a significant reduction in the amplitude of SENS (reduced to  $121.3 \pm 1.9 \mu\text{m}$ ,  $n = 38$ ,  $p < 0.001$ ) but not in LEVR ( $124.8 \pm 1.9 \mu\text{m}$ ,  $n = 27$ ,  $p = 0.39$ , Figure 2.5). 1  $\mu\text{M}$  levamisole reduced the amplitude of SENS by 10.3% but the LEVR amplitude did not decrease.

When we examined *H. glycines* to test for species variation, we found that it had a much smaller amplitude contraction wave than the *O. dentatum* larvae. *H. glycines* had a mean amplitude of  $89.6 \pm 1.8 \mu\text{m}$  (mean,  $\pm$  s. e.,  $n = 150$ ) which was significantly smaller than the SENS and LEVR isolates ( $p < 0.001$ ).

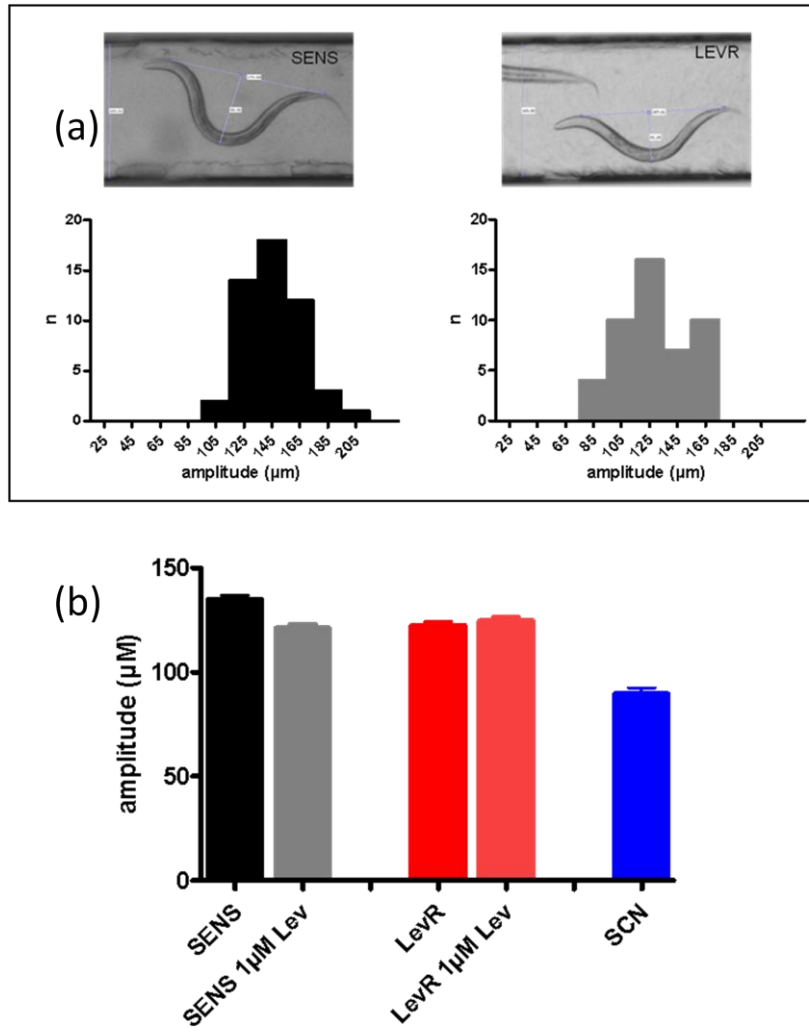


**Figure 2.5:** (a) Statistical distribution of the measured amplitude for SENS and LEVR *O. dentatum* larvae is shown. The difference in amplitude is also visible in the two snapshots of the *O. dentatum* larvae. (b) The measured amplitude are depicted for SENS and LEVR larvae without any drug exposure, SENS and LEVR larvae exposed to 1 $\mu\text{M}$  levamisole, and *H. glycines* nematodes.

### 2.3.2 Wavelength Measurements

SENS had a mean wavelength of  $372.9 \mu\text{m} \pm 7.1 \mu\text{m}$  (mean,  $\pm$  s. e.,  $n = 32$ ) and LEVR had a mean wavelength of  $393.1 \pm 4.6 \mu\text{m}$  (mean,  $\pm$  s. e.,  $n = 35$ ) which was



significantly different ( $p = 0.019$ ), as shown in Figure 2.6. 1  $\mu\text{M}$  levamisole did not have a statistically significant effect on the wavelengths of either of the isolates.

The mean wavelengths of *H. glycines* was  $310.2 \pm 3.3 \mu\text{m}$  (mean,  $\pm$  s. e.,  $n = 150$ ), as shown in Figure 2.6. The wavelength of the SENS isolate is significantly larger than the wavelength of *H. glycines* ( $p < 0.001$ ). The smaller wavelength for *H. glycines* is consistent with the smaller size of the plant parasite compared to the slightly longer length of the *O. dentatum* larvae.

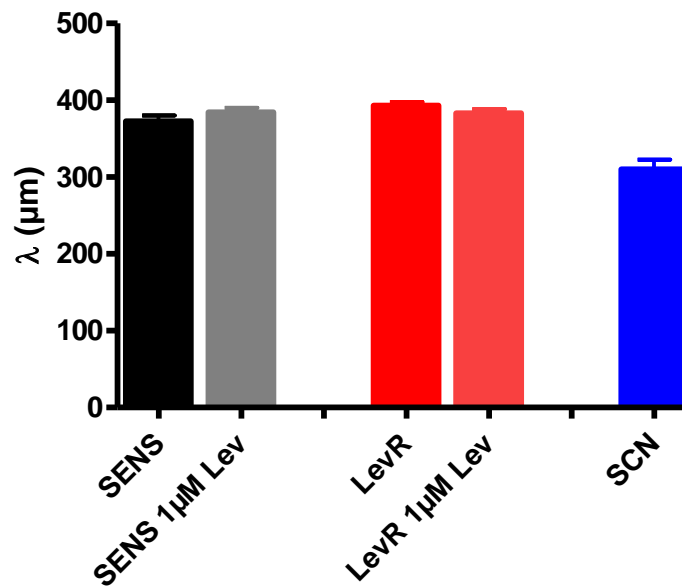


**Figure 2.6:** The measured wavelength is shown for SENS and LEVR *O. dentatum* larvae without any drug exposure, SENS and LEVR *O. dentatum* larvae exposed to 1  $\mu\text{M}$  levamisole, and *H. glycines* SCN nematodes. There is no significant difference in wavelength between SENS and LEVR larvae with or without exposure to levamisole. The SCN nematodes are physically smaller than *O. dentatum* larvae and thus demonstrate a shorter wavelength.

### 2.3.3 Tangential Force for Forward Movement

An interesting aspect of the nature of nematode locomotion involves the role of both amplitude and wavelength, which had initially motivated us to measure these body parameters. In 1953, Gray [23] has reported a detailed theoretical analysis of undulatory motion. He derives the maximum forward tangential force,  $F_T$ , exerted by a half-wave of the nematode body and relates to its body parameters. This normalized force  $F_T / W_o$  is expressed as [23, 25]:

$$\frac{F_T}{W_o} = \frac{2\pi A/\lambda}{\lambda\sqrt{1+(2\pi A/\lambda)^2}} \quad \text{Equation (2.1)}$$

This force is directly related to  $A/\lambda$ . The normalization coefficient  $W_o$  in Equation (2.1) depends on parameters such as surface tension, frictional force, and coupling moment which are assumed unchanged in our experiments [23]. To clarify, the coefficient  $W_o$  has the unit of  $N \cdot m$ . As shown in Figure 2.7, the body of a nematode can be viewed as different segments where each individual segment applies a tangential force  $F_T$  for the forward propulsive motion. The above equation also implies that this tangential force increases with increase in amplitude and decrease in wavelength [23]. The data gathered for our amplitude and wavelength analysis were used to obtain a set of  $A/\lambda$  quotients.

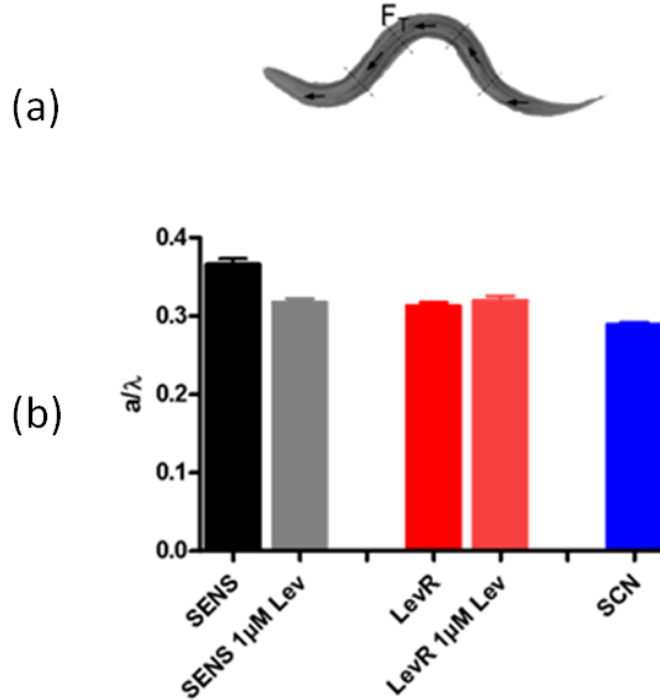


**Figure 2.7:** (a) The tangential force  $F_T$  exerted by each segment of the nematode's body results in the characteristic sinusoidal movement. (b) The amplitude to wavelength ratio is plotted for SENS and LEVR larvae without any drug exposure, SENS and LEVR larvae exposed to 1 $\mu$ M levamisole, and *H. glycines* SCN nematodes. The SENS larvae has a higher amplitude to wavelength ratio than that for LEVR larvae which is significantly decreased during exposure to levamisole. This ratio is relatively unchanged for LEVR larvae after exposure to levamisole. The SCN nematodes have a lower amplitude to wavelength ratio compared to *O. dentatum* larvae.

The mean  $\pm$  s.e.  $A/\lambda$  quotient values of experiments on *O. dentatum* larvae and *H. glycines* are shown in Figure 2.7(b). The mean of  $A/\lambda$  quotients for the SENS isolate was  $0.366 \pm 0.007$  (mean  $\pm$  s. e.,  $n = 32$ ), while that for the LEVR isolate was  $0.313 \pm 0.005$  (mean  $\pm$  s. e.,  $n = 35$ ) which is significantly smaller ( $p < 0.0001$ , unpaired t-test). After exposure to 1  $\mu$ M levamisole, the mean  $A/\lambda$  quotient of SENS isolate showed a 13% decrease to  $0.317 \pm 0.005$  (mean  $\pm$  s. e.,  $n = 38$ ) whereas the LEVR isolate showed a 4.6% increase to

$0.327 \pm 0.006$  (mean  $\pm$  s. e.,  $n = 27$ ). The decrease in  $A/\lambda$  quotient for the SENS isolate was significant ( $p < 0.001$ ) while there was no statistically significant difference in the  $A/\lambda$  quotient for the LEVR isolate with  $1 \mu\text{M}$  drug exposure ( $p > 0.05$ ).

Following Equation (2.1), the mean of the normalized tangential force for the SENS isolate was  $2.49 \pm 0.05 \times 10^{-3}$  (mean  $\pm$  s. e.,  $n = 32$ ) while that for the LEVR isolate was significantly smaller ( $p < 0.001$ ),  $2.27 \pm 0.03 \times 10^{-3}$  (mean  $\pm$  s. e.,  $n = 35$ ). After exposure to  $1 \mu\text{M}$  levamisole, the mean normalized force of the SENS isolate showed a 6.0% decrease to  $2.34 \pm 0.04 \times 10^{-3}$  (mean  $\pm$  s. e.,  $n = 38$ ,  $p < 0.02$ ) whereas the LEVR isolate showed no significant change and was  $2.36 \pm 0.04 \times 10^{-3}$  (mean  $\pm$  s. e.,  $n = 27$ ,  $p > 0.05$ ). The percentage changes in the mean normalized force among the *O. dentatum* isolates follow a similar trend as reflected previously by percentage changes in their  $A/\lambda$  quotient values. This reiterates that the tangential force needed for the forward movement is directly proportional to the  $A/\lambda$  quotient and is an important locomotion parameter for segregating nematodes of different isolates and their response to drugs.

Examination of the  $A/\lambda$  and tangential force results among the *O. dentatum* isolates leadsto interesting implications. A significantly lower  $A/\lambda$  quotient for the LEVR isolate compared to the SENS isolate indicates less forward locomotive force, and suggests that the resistance to levamisole in LEVR has lowered its vigor. We estimated  $F_T$  using Equation 2.1 to check and confirmed that it was significantly reduced in LEVR. In the presence of levamisole, the  $A/\lambda$  quotient of the SENS isolate was significantly decreased but the quotient of the LEVR isolate was not. The observation indicates that the SENS isolate, following levamisole treatment, has less propulsive force but LEVR is not significantly affected. This

result is consistent with the larval migration studies [20] where SENS is inhibited more than LEVR by levamisole. We expect that the tangential force exerted by the different segments of the nematode body is proportional to the amount of muscle contraction actively generating forward movement. Since the cholinergic anthelmintic levamisole affects body muscle contraction, it is not surprising that we have observed distinct differences in the locomotory parameters of SENS and LEVR *O. dentatum* larvae when exposed to levamisole.

We also examined  $A/\lambda$  quotient for *H. glycines*. The  $A/\lambda$  quotient of *H. glycines* was  $0.289 \pm 0.008$  (mean  $\pm$  s. e.,  $n = 150$ ). An unpaired t-test ( $p < 0.001$ ) between the  $A/\lambda$  quotients of the SENS isolate and *H. glycines* revealed a significant difference. The mean of the normalized tangential force for *H. glycines* was  $2.84 \pm 0.03 \times 10^{-3}$  (mean  $\pm$  s. e.,  $n = 150$ ) which was 13.7% greater than that for the SENS isolate. A larger normalized force for *H. glycines* compared to SENS isolate is due to their much shorter wavelength. This also indicates that while comparing two nematode species with significantly different wavelengths (e.g. *O. dentatum* larvae and *H. glycines*), the normalized tangential force is closely related to their individual wavelengths besides their  $A/\lambda$  quotients. Whereas, isolates within the same species (e.g. SENS and LEVR *O. dentatum* larvae) may usually have statistically insignificant differences in wavelength and thus the normalized tangential force will be closely related only to the  $A/\lambda$  quotients.

### 2.3.4 Velocity Measurements

We compared the forward velocities of the *O. dentatum* larvae with increasing concentration of levamisole, as shown in Figure 2.8. In the absence of levamisole, the SENS isolate had a velocity of  $149.25 \pm 6 \mu\text{m s}^{-1}$  (mean  $\pm$  s. e.,  $n = 31$ ). LEVR had a velocity of 143

$\pm 4 \mu\text{m s}^{-1}$  (mean  $\pm$  s. e.,  $n = 37$ ). The velocities of both SENS and LEVR larvae were each measured on the same three days. There was no statistically significant difference between the velocities of SENS and LEVR isolates in the absence of levamisole.

*H. glycines* had a velocity of  $28.1 \pm 2.0 \mu\text{m/s}$  (mean  $\pm$  s. e.,  $n = 20$ ) which was significantly smaller than the isolates of *O. dentatum* larvae and *H. glycines* ( $p < 0.0001$ , unpaired t-tests). The much slower speed of *H. glycines* was expected because plant nematodes do not need to move rapidly searching for their plant hosts in contrast to the animal parasites.

Next, we tested the effect of different concentrations of levamisole on the SENS and LEVR *O. dentatum* larvae. We measured the forward velocity of SENS and LEVR isolates when exposed to levamisole. The velocities at various drug concentrations are plotted in Figure 2.8. There was little decrease in velocity for either SENS or LEVR isolates at a levamisole concentration below  $0.5 \mu\text{M}$ . However, the SENS velocity drops clearly reduces with  $1 \mu\text{M}$  while a similar reduction in velocity for LEVR requires a levamisole concentration of  $3 \mu\text{M}$ . The EC50 for SENS isolate was  $3 \mu\text{M}$  and the EC50 for LEVR isolate was  $10 \mu\text{M}$  as shown in Figure 2.8. Thus, we obtained a resistance ratio of three between the two isolates as measured from the forward velocities on the microfluidic device. From previous migration studies [20], the SENS EC50 was  $26 \mu\text{M}$  and the LEVR EC50 was  $114 \mu\text{M}$ . This indicates that the microfluidic device has roughly a ten-fold better sensitivity compared to the migration assay [22] but the resistance ratio between SENS and LEVR is similar in both cases.

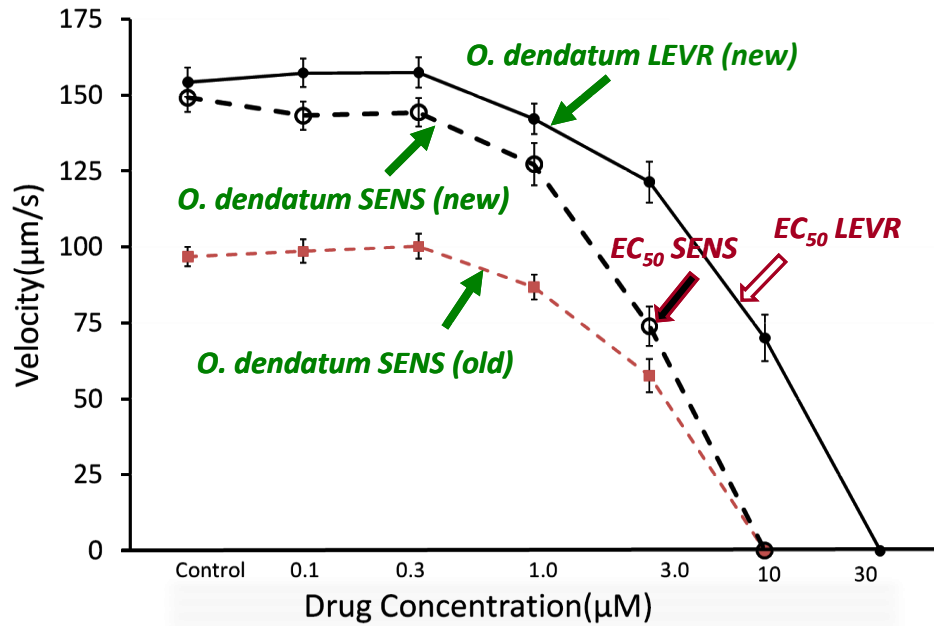


**Figure 2.8:** Velocity measurements. The measured forward velocity for SENS (dashed) and LEVR (solid) *O. dentatum* are plotted with increasing concentration of the drug levamisole. After a drug concentration higher than 1 µM, the velocity of SENS isolate decreases significantly whereas the velocity of LEVR isolate decreases significantly at a drug concentration higher than 3 µM. The EC<sub>50</sub> for SENS isolate is 3 µM while the EC<sub>50</sub> for LEVR isolate is 9 µM. The plant parasitic *H. glycines* is much slower in its forward movement compared to the animal parasitic *O. dentatum* larvae (not shown in the figure).

### 2.3.5 Frequency Measurements

Frequency analysis was carried out to further test measurements of velocity and wavelength. As an additional and separate test, velocity data and wavelength data were collected independently from different videos. The predicted frequency for all nematode sets was estimated by dividing the mean velocity by mean wavelength. The observed frequency was determined by observing image frames, measuring the actual time taken by the nematode larvae to return to its original state (i.e. measure the time period), and then taking the inverse of this time period. We found that the predicted frequency values were close and not

significantly different to the observed frequency values. Interestingly, these observations were consistent with a classical equation of physics (velocity = wavelength  $\times$  frequency) and this equation was found to be valid when describing the undulatory movement of nematodes, up to the limit of the resolution for our recording system.

The *O. dentatum* SENS larvae had an observed mean frequency of  $0.35 \pm 0.02$  Hz (mean  $\pm$  s. e.,  $n = 75$ ) which was not significantly different from the mean frequency of LEVR which was  $0.38 \pm 0.02$  Hz (mean  $\pm$  s. e.,  $n = 75$ ). However, 1  $\mu$ M levamisole reduced the frequency of SENS by 23 % to  $0.27 \pm 0.02$  Hz,  $n = 25$  ( $p < 0.001$ ) but produced little change in the LEVR isolate ( $0.35 \pm 0.02$  Hz,  $p > 0.1$ ). *H. glycines* had a mean frequency of  $0.127 \pm 0.002$  Hz,  $n = 75$ , which was significantly less ( $p < 0.001$ ) than *O. dentatum* SENS.

### 2.3.6 Worm Image Tracking Program

The videos recorded during the experiments on drug dose response are analyzed with the an imagine tracking program. The output image file provided screenshots of the body dimensions and paths traversed as shown in Figure 2.9(a). Parameters such as wavelength, amplitude, forward velocity, and track signatures were extracted from the output file. As shown in Figure 2.9(b), a series of video processing steps were done on the input video file to minimize the background noise, improve the image resolution, and further process the relevant data.

An interesting aspect of the drug effect on the worm's movement is demonstrated in Figure 2.10. Here, two-dimensional paths traversed by representative SENS and LEVR worms at various levamisole concentrations are plotted as extracted from the worm tracking program. In the control experiments, body centroid of both SENS and LEVR isolates



followed a relatively straight path in the x direction with minimal deviation in the y direction. As the levamisole concentration reached 1  $\mu\text{M}$ , the SENS isolate showed a greater deviation in the y direction compared to the LEVR isolate, while the track lengths were comparable for both of them. At 3  $\mu\text{M}$  levamisole, the SENS appeared drugged with very frequent halts and turnarounds while the LEVR still showed resilience to the drug but with increased deviations in the y direction. At 10  $\mu\text{M}$  levamisole, the SENS were completely paralyzed while the LEVR's movement had much more frequent halts and turnarounds compared to lower concentrations. The track signatures of nematodes plotted in Figure 2.10 provide a simple, graphical schematic of the steadily deteriorating effects of drugs on the worms' movement. This figure adequately complements the graph in Figure 2.9b which gives the actual values of a motility parameter (i.e. average forward velocity) as the nematode's sinusoidal movement deteriorates with drug exposure.

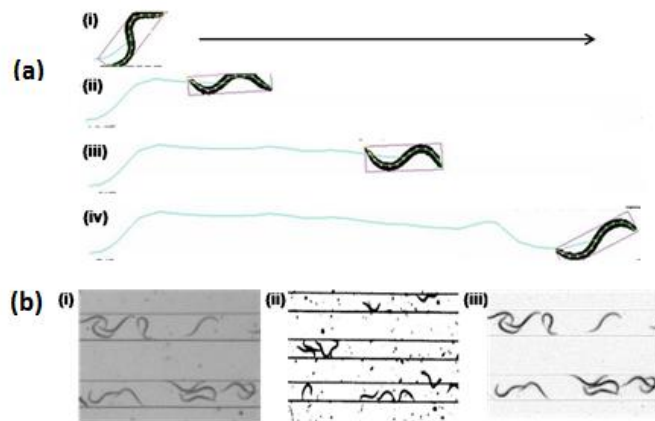


**Figure 2.9:** Video processing and extraction of motility parameters using an image-tracking program. (a) The worm body is segmented into thirteen splines and the body centroid is tracked over the time duration of its forward movement. The program encloses the worm in a rectangular box and keeps record of the changing box dimensions as the worm moves in the microfluidic channel. (b) Sequence of steps in processing the raw videos involves background negation, channel segmentation, and worm recognition.

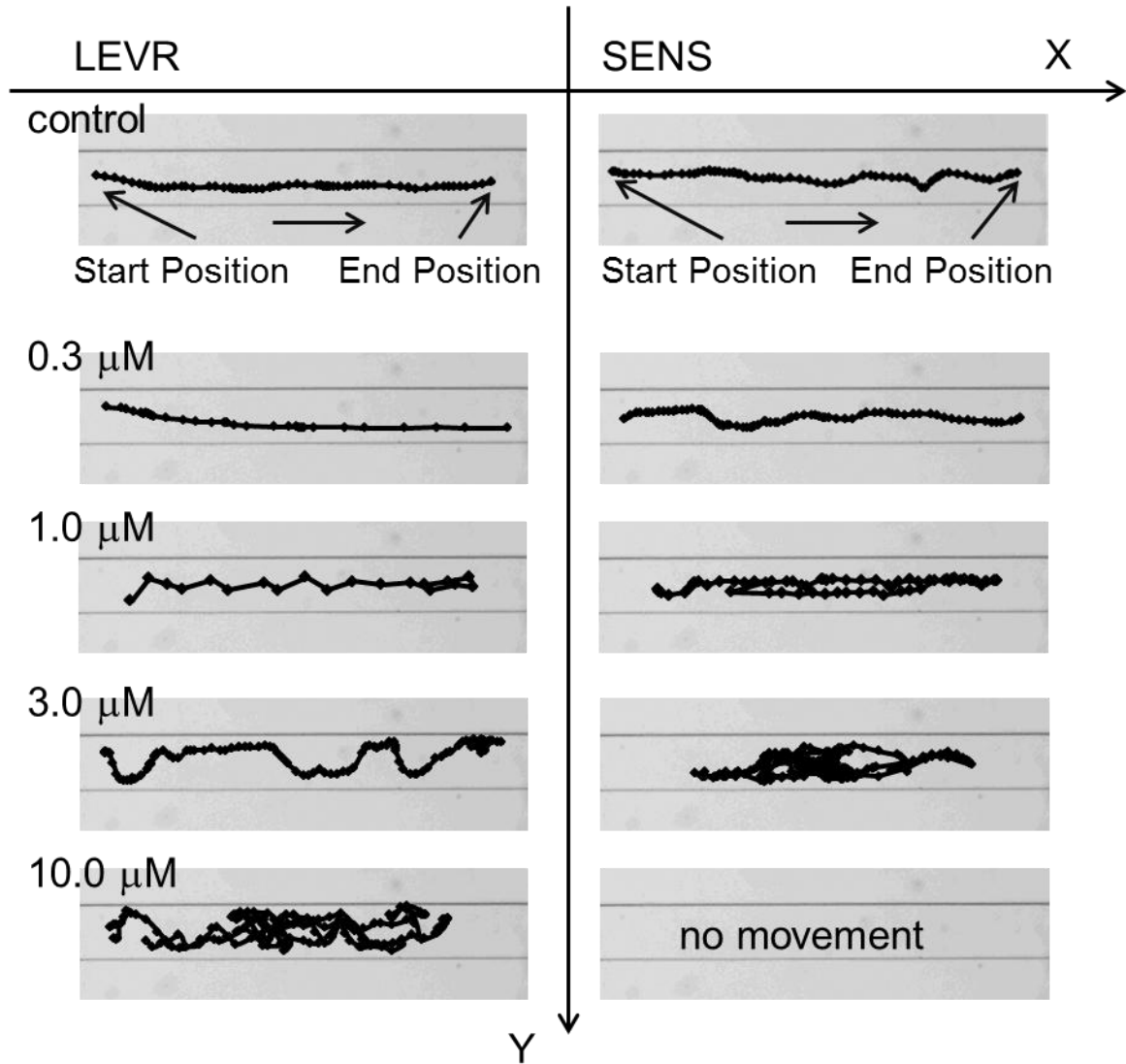


**Figure 2.10:** Individual worm tracks of *O. dentatum* nematodes obtained from the image-tracking program. Without any drug exposure, the SENS and LEVR move in a relatively straight x-direction with insignificant movement in y-direction. With increasing levamisole concentration (e.g. 1  $\mu\text{M}$ ), their movement starts becoming zigzag with noticeable component in y-direction. At 3  $\mu\text{M}$  levamisole, the SENS are almost paralyzed with erratic movement and frequent turnarounds while the LEVR is still able to exhibit its natural forward movement but with increased sloppiness. At 10  $\mu\text{M}$  levamisole, the SENS are completely paralyzed and unable to enter the microfluidic channels while the LEVR are almost paralyzed with significantly erratic forward movement and frequent turnarounds.

## 2.4 Discussion

We presented a microfluidic device with parallel straight channels to observe and characterize nematode locomotion parameters. We demonstrated that these locomotion parameters are different for *H. glycines* (the soybean cyst nematode), and the SENS and LEVR isolates of *O. dentatum*. Furthermore, we demonstrated the use of the microfluidic device for observing drug effects on targeted nematode isolates with better sensitivity than migration assays. Our approach is attractive because it allows us to run multiple experiments (each in an individual channel) simultaneously and record the nematode movement from all the channels. The low cost of device mass production renders them disposable [38] although they can be re-used multiple times.

The locomotion studies described thus far can be conducted in channels filled with water or any suitable fluids. We preferred to use agar-filled channels for the following reasons: (a) Agar provides a better medium for the worms to push against as they crawl and propel themselves forward. In a fluid environment, the worms will swim and encounter slips as they move forward. As such, a solid agar medium would be closer to the natural soil habitat of these worms. (b) In microfluidic channels, it is difficult to maintain constant fluid pressure when both sides of the channel are exposed to air. In our initial experiments with water as a medium, the fluid pressure in the channel interfered with the natural movement of the nematodes. Such variation in fluid pressure is not a concern when using agar or other gel-like material as a medium in the channels.

Besides illustrating the difference in movement phenotype between the drug-sensitive and drug-resistant isolates, we think the usefulness of the microfluidic device also lies in

drug testing. Currently, worm migration assays based on mesh structures are used to characterize the effect of a drug on nematodes [20]. The testing is a slow process taking a few hours, having thousands of nematodes for a single test, requiring higher concentrations of the drug, and with no scheme for parallelization. With the microfluidic devices presented here, the drug testing was done in parallel and each test was completed within 45-60 minutes. Compared to the binary migrated/inhibited or hatch/not hatch measurements used in larval migration or egg hatch assays, we are able to measure the nematode velocity, wavelength, and amplitude in the microfluidic device. Furthermore, the drug sensitivity is significantly improved. We have shown that the EC50 for the *O. dentatum* larvae on the microfluidic device is roughly 10 times smaller than that measured for *O. dentatum* larvae on the migration assays, as shown in Figure 2.8. However, with higher levamisole concentrations, the forward movement of the larvae in the micro channels becomes more sluggish and discontinuous. Figure 2.11 shows the upper limit of the levamisole dose that was useful for *O. dentatum* larvae in the microfluidic device. At a dose of 2.2  $\mu\text{M}$  of levamisole, the SENS isolate lost some of its ability to make sinusoidal movements but LEVR retained this capacity. As shown in Figure 2.8, the forward velocity can still be measured in and above this range concentration of drug, until the larvae is completely paralyzed. This drug concentration limit is reached at 10  $\mu\text{M}$  of levamisole for the SENS isolate and at 30  $\mu\text{M}$  for the LEVR isolate.

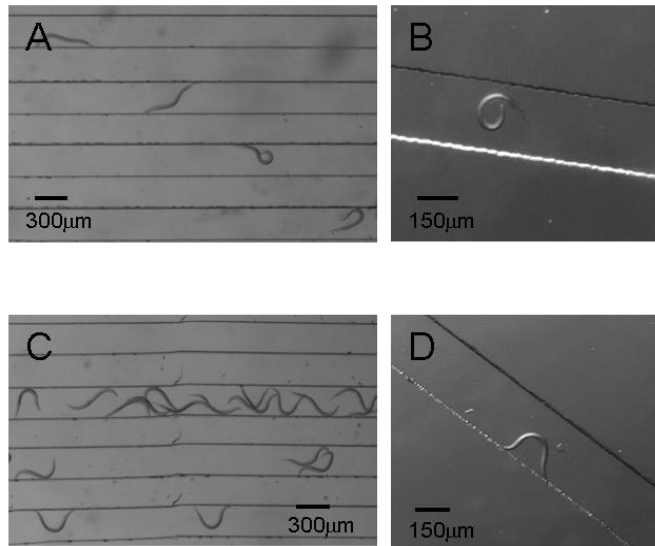


**Figure 2.11:** There are distinct changes in the locomotion patterns of *O. dentatum* larvae in the microfluidic device at higher concentrations of levamisole (above 3  $\mu\text{M}$ ). (A, B) Upon exposure to 5  $\mu\text{M}$  levamisole, the natural sinusoidal movement of SENS larvae is distorted with longer migration time, occasional curling, and retraction from forward movement. (C, D) At the same drug concentration, the movement of LEVR larvae is not perturbed with insignificant changes in their locomotion parameters.

Although our focus for this study was on the detection and characterization of the phenotypes of parasitic larvae that are associated with anthelmintic resistance, the methods are also likely to complement reverse genetic experiments where gene knockdown, knockout or transgenic experiments [20] may produce subtle locomotory phenotypes.

The time required for data analysis and parameter extraction will be significantly improved by using automated nematode tracking software. Several groups have developed such worm tracking software that automatically calculates parameters such as forward velocity, oscillation frequency, and body bending for *C. elegans* [31, 39, 40]. Currently, we use MATLAB to calculate body parameters which takes considerable amount of time. As the next step, we are working towards automating the entire data recording and analysis steps by

adding a movable test stage and developing a user-friendly program for tracking nematodes in the micro channels and extracting their locomotion parameters.

We point out that, as with any bioassay, our method has potential sources of error. A number of factors need to be controlled and be minimized to have minimal error. For example, movement of the larvae will be reduced by a temperature reduction. This requires that collection of the data for comparison be made at the same temperature. We also found that as the age of the larvae increased, there was a gradual decrease in the velocity of movement; thus variation between isolates, even those that are drug sensitive may be anticipated. However, we do expect that despite some phenotypic variation between drug-sensitive isolates, that they will show sensitivity to the drug under test, in contrast to the resistance isolates. Despite potential limitations, we think that these sources of error can readily be controlled for and that our microfluidic assay offers an improved and higher level of resolution compared to worm migration assays.

## Chapter 3

### Automated Screening of Nematodes in Sinusoidal Microfluidic Channels

#### 3.1 Introduction

As introduced in Chapter 2, nematodes such as *O. dentatum* and *C. elegans* inherently move in a sinusoidal manner [30]. Today, there are various new strains of these nematodes either created by genetic modifications or naturally occurring in the soil environment. As discussed in Chapter 2, some of these strains can be distinguished from one another by carefully observing differences in their locomotion parameters. Our work in straight channels was motivated by a drive in the scientific community for new high-throughput worm screening and sorting platforms. In the various worm sorters reported, researchers primarily immobilized (by suction or cooling) the organism in microchambers to record time lapsed images of the worm body. Computer programs analyzed the images to give information of the worm type based on measured body parameters (such as amplitude, wavelength). In such devices, the use of anesthesia is avoided which may induce long-term effects on the worm physiology.

In this chapter, we proposed a simple and new method of automatically sorting various strains of a certain nematode species. Unlike previous devices that use sophisticated algorithms to control worm transport and the microfluidic valves, the proposed design requires no moving components and is entirely passive in operation. Here, sinusoidal channels are fabricated using soft lithography technology and nematodes are allowed to pass through channels. The thickness of the sinusoidal channel is adjusted to be slightly greater than the thickness of the worm body. Extensive tests were conducted on several designs of

sinusoidal channels varying in amplitude and wavelength. Designs were also created where the amplitude (amplitude modulated AM) or the wavelength (frequency modulated FM) changed gradually along the length of the chip. We focused on two different isolates of the *Oesophagostomum dentatum* (levamisole-sensitive SENS and levamisole-resistant LEVR). Our hypothesis was that worms whose natural amplitude and wavelength matched that of the sinusoidal channel would move faster through that section. Beyond the ‘adaptable range’, the worms would find it difficult to push forward and would eventually retract or stay immobile. Based on our result summarized in Chapter 2 [22], the locomotion parameters of the nematode’s sine-waves are directly related to the phenotype, age and vigor of the worms. We would expect that different nematode strains (that even though are visually indistinguishable) would show distinct movement patterns through the sinusoidal channels. By defining a number of parameters (e.g. cut-off region, stopping probability, average velocity), we would be able to segregate and sort different strains.

The original idea of putting nematodes in sine-wave channel of fixed dimensions was introduced by Lockery’s group [25] where they showed that *C. elegans* can adapt to different dimensions of channels. Their work was mainly focused on introducing the idea of ‘artificial dirt’ and microfluidic devices to the nematode community and their work was limited to sinusoidal channels with fixed parameters. Extending this work, we designed a broad range of sinusoidal channels, defined a set of locomotion parameters for the fixed sine-wave device, and proposed modulated sine-wave channels with a new application on screening and sorting nematode strains. To automate the process of data extraction and analysis, an image tracking



software was developed to collect and analyze the large amount of data. Detailed data analysis shows the practical use of the developed system as a simple worm sorter.

## 3.2 Fixed Sine-wave Devices

### 3.2.1 Sinusoidal Channel Designs

#### Design 1

A sinusoidal wave has two parameters: wavelength ( $\lambda$ ) and amplitude (A). To fabricate a microfluidic channel shaped as a sine-wave, two additional parameters are required: channel horizontal width and vertical height. The optimal dimensions of the amplitudes and wavelengths were obtained from our previous work on wavelength and amplitude characterization [22]. We reported a wavelength of  $372.9 \pm 7.1 \mu\text{m}$  (mean,  $\pm$  s. e.,  $n = 32$ ) and  $393.1 \pm 4.6 \mu\text{m}$  (mean,  $\pm$  s. e.,  $n = 35$ ) for SENS and LEVR respectively. The body width of *O. dentatum* is around  $18 \mu\text{m}$  [22]. Based on this information, we selected a set of amplitude and wavelength combinations for designing the sine-wave devices. The wavelengths were chosen to be  $132 \mu\text{m}$ ,  $198 \mu\text{m}$ ,  $264 \mu\text{m}$ ,  $330 \mu\text{m}$ ,  $396 \mu\text{m}$  and  $462 \mu\text{m}$ ; each with an increment of  $66 \mu\text{m}$ . The amplitudes are chosen as  $60 \mu\text{m}$ ,  $120 \mu\text{m}$  and  $240 \mu\text{m}$ . The channel width was chosen to be wide enough to allow smooth passage of the worm body but narrow enough to limit the errors in maximum channel wavelength and amplitude. The sine-wave channel width is set at  $30 \mu\text{m}$ . The combination of 18 ( $=6 \times 3$ ) of different wavelengths and amplitudes were designed using AutoCAD and sent to a commercial vendor (Fineline Imaging, Colorado Springs, CO) for mask generation. As shown in Figure 3.1, each design accommodates three different wavelengths in one channel. Figure 3.2 shows a set of snapshots of fabricated devices.

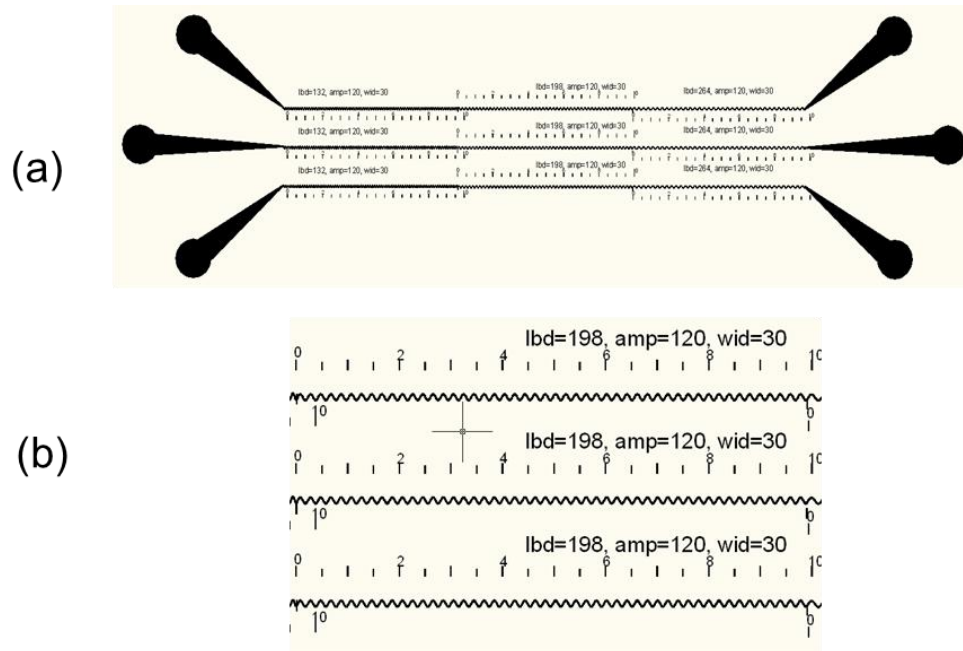


**Figure 3.1:** Fixed Sine-wave Channels: (a) an overview of a sine-wave chip. It includes 3 identical channels, each consisting of 3 sections with different wavelengths. There are input and output ports on either side of the device for worm entrance and exit. (b) A sample sine-wave with wavelength of 198  $\mu\text{m}$ , amplitude of 120  $\mu\text{m}$  and channel width of 30  $\mu\text{m}$ .

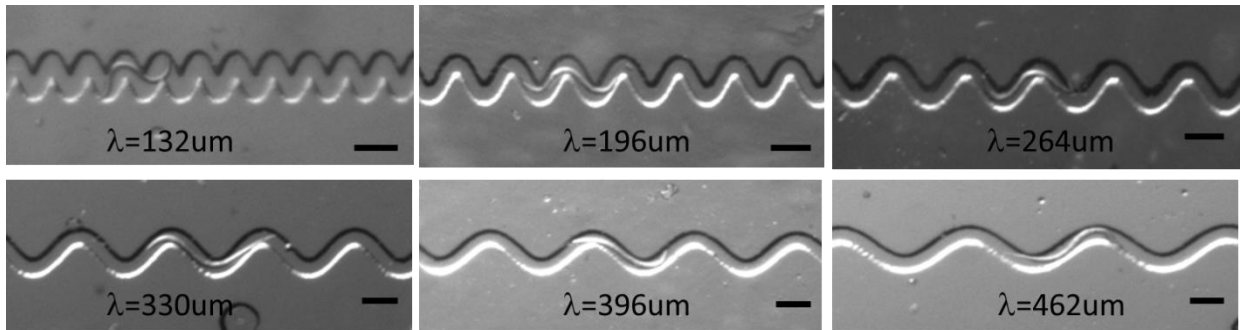


**Figure 3.2:** A set of snapshots of a single nematode confined in sine-wave channel of fixed amplitude and changing wavelengths. The amplitude here is 120  $\mu\text{m}$ .

### Design 2:

The previous design of three identical sine-wave channels in a chip provided a basis for conducting rigorous high-throughput tests on nematodes. From the preliminary experiments, we realized the limitations of design 1. These sine-wave channels confined the movement of the nematodes in a restricted space. But this confinement also limited the number of worms that could be observed in a single experiment. This is because the worms prefer to move in unrestricted channels (similar to straight channels in Chapter 2) rather than in confined sine-wave trenches. This reduced the experimental throughput and reduced the number of samples available for a given test run. We focused our efforts on improving the testing efficiency.

We discovered several ways to reliably insert the worms into the sine-wave channel and allow them to continue with forward movement. One of the ways which proved effective was to use of a syringe to pull the solution from the output port of the channel while the nematodes were kept in the input port. The method proved to be effective and repeatable. However, during this mechanical suction, the nematodes have the potential of getting injured by the high suction pressure. As a result, this method could not conserve the viability of the worms and could likely affect the experimental result. To make sure worms are still viable and moving in a natural manner, a passive method of worm insertion was required.

For certain species of parasitic nematodes, there are specific attractants or deterrents (such as food or citric acid) to entice the worms to explore into the channel. However, this would add additional chemicals into the worm's body which may have an unknown effect on its natural movement. We wanted to avoid the use of any external chemical factors.

To increase the time efficiency and throughput of the experiment, a simple approach would be to increase the number of sine-wave channels per chip. Considering the fact that the cost of chip fabrication is relatively cheap, the maximum area of the chip was decided based on the maximum field of view under the microscope. We sought to increase the density of devices on a single chip by efficiently using the total area.

As in previous designs, the maximum density of channels in one single chip is decided by the area occupied by the input/output ports. These ports serve as a connection to the outside world (with syringe and tubing) and cannot be easily scaled down. In our experiments, the design rule sets the port diameter as 2 mm in and with an inter-port spacing of 5 mm. We proposed a design having multiple channels sharing a single input/output port, as shown in Figure 3.3. This mitigates the design limitations set by the size of individual ports. With this approach, we were able to pack much more channels into one single chip and increase the experiment efficiency and throughput. In this structure, the upper limit on the number of channels per port is set by the design rule of the mask (i.e. the minimum spacing between adjacent channels).

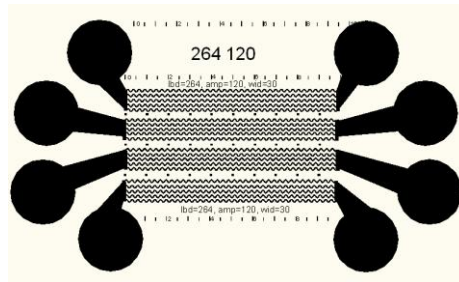


**Figure 3.3:** High throughput chip with sinusoidal wave channel (design 2). In this graph, we show 5x4 channels packed in a single chip. Five channels share one same input/output port. This increases the throughput of the chip by seven times (from 3 channels per chip in design 1 to 20 channels per chip in design 2).

### 3.2.2 Device Fabrication

The microfluidic devices were designed to have multiple sinusoidal wave channels; each set of five channels with its individual input and output ports. The device dimensions can be easily altered at the design stage to be adapted to a certain species of nematodes and the desired experimental goal.

The device fabrication is done using standard micromachining and soft lithography procedures [38]. The mask layout is designed in AutoCAD and sent to an outside vendor (Fineline Imaging, Colorado Springs, CO) to generate the masks. A 40  $\mu\text{m}$ -thick SU-8 photoresist (Microchem Corporation, Newton, MA) is cast on a bare three-inch silicon wafer by spin coating at 1000 r.p.m..

Compared with the structure reported previously in Chapter 2, the fabrication of the device is carried out with carefully controlled parameters as the channels are not straight and device density is increased significantly. The upper limit of the packing number of the channels into a given region is mainly set by the photo resistor used and the aspect ratio. The exposure time was carefully adjusted to prevent any overexposure or underexposure of the SU-8. The post-exposure baking time is adjusted to provide adequate adhesion to the silicon wafer while still keeping it susceptible for SU-8 development. A hard bake step after the development step was often required to improve the adhesion of the SU-8 to the silicon substrate.

The PDMS pre-polymer (Sylgard-184 Silicone Elastomer Kit, Dow Corning Corporation, Midland, MI) was cast over the SU-8 mold and cured on a hot plate at 70°C for two hours. Subsequently, the PDMS microfluidic devices were peeled off the mold and

input/output ports (2 mm diameter) were created using a sharp needle. The PDMS device and glass cover slip were then treated with methanol spray to modify the surface property from hydrophobic to hydrophilic. After methanol treatment, air plasma was used to expose PDMS devices and glass cover slips, both of which are then bonded together. One of the masks is shown in Figure 3.3. One of the fabricated microfluidic chips is shown in Figure 3.4 along with nematodes moving through the sealed sine-wave channels.

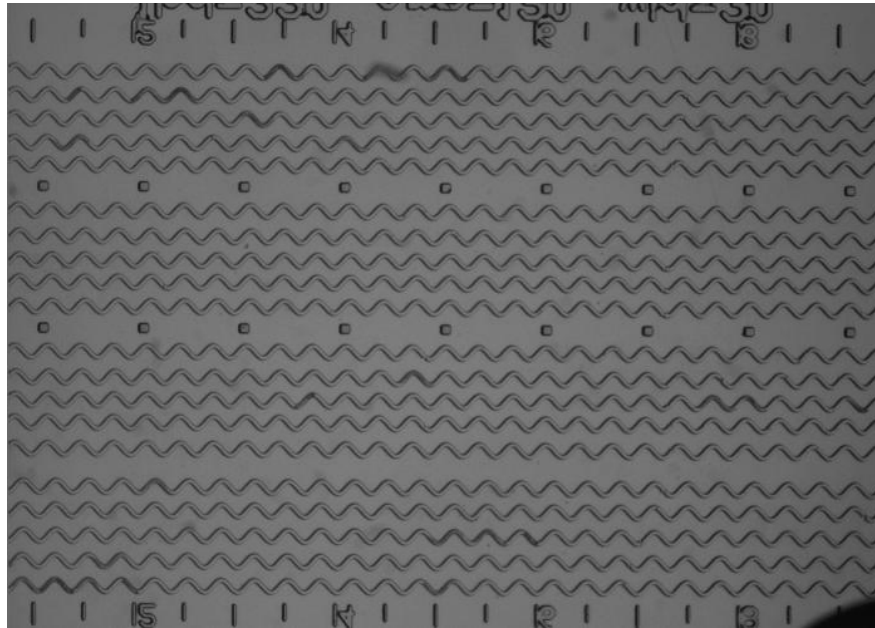


**Figure 3.4:** Microphotographs of fabricated sine-wave channels in an experiment. The wavelength is at 330  $\mu\text{m}$  and the amplitude is at 120  $\mu\text{m}$ . Five channels share one input/output ports (not shown in figure) to efficiently utilize of the chip area without compromising the image resolution and field of view. A total of 20 sine-wave channels are packed in one device to increase the experimental throughput. On-chip markers and rulers are included for calibration purpose.

### 3.2.3 *O. dentatum* Larvae as Test Nematodes

Levamisole-sensitive (SENS) and levamisole-resistant (LEVR) *O. dentatum* used in the experiment is the same as in Chapter 2. The culture and preparation of these biological

samples is discussed previously. It is worth mentioning that the bodies of both isolates (SENS and LEVR) are visually indistinguishable under a microscope and, in nature, there are apparently more strains of the *O. dentatum* species with varying levels of drug resistance. Our goal is to devise a method to automatically distinguish these isolates passively (without the application of any chemicals) by passing them through sine-wave channels and observing them at real-time.

### 3.2.4 Sample Preparation and Loading

A small volume (1mL) of nematode solution was pipetted and centrifuged at the speed of 3000 r.p.m. to increase the worm density to about 100/ $\mu$ L. Later, around 0.36  $\mu$ L of worms was pipetted and filled into each of the four input ports of the microfluidic device. Care was taken to ensure that input ports of the channels do not trap any air bubbles. Air bubbles block the path of nematodes and can aggregate or migrate in the microchannels. After 5 to 15 minutes (the scouting time), the nematodes enter the sine-wave channels from the input ports and moving through the channel towards the output ports.

### 3.2.5 Data Capture and Analysis

Similar to the instrumentation used in Chapter 2, the nematodes were observed with a Leica MZ16 transmission stereomicroscope using magnifications from 7.1x to 230x. In this experiment, the magnification is set at 1.25x10. A QICAM 12-bit Mono Fast 1394 Cooled digital camera interfaces with a QCapture Pro software for capturing individual digital images and image sequences. Image sequences of nematode movement were recorded at a time interval of one second and with a resolution of 1392 x 1040 pixels. The recorded videos were saved in uncompressed .avi video format. These videos were later imported into a

custom image tracking software where individual frames are analyzed. The details of the tracking software are described in Appendix1. An actual distance to pixel distance ratio was calculated by measuring the pixel width of a channel of known width using the QCapture Pro software toolbox. This ratio was used to translate pixel measurements to actual distance for the calculation of nematode velocity, amplitude and wavelength.

### 3.2.6 Calculation of Locomotion Parameters

Nematodes with unimpeded forward propagation exhibit a consistent velocity over distances much longer than their body length. Worm average velocity is defined here as ratio of the continuous forward linear distance traveled by the nematode's centroid to the time duration. In our experiments, the videos were analyzed using the custom program to produce a ".csv" file containing data sets of worm's centroid position as a function of lapsed time. This data set of centroid position is used to plot the track of an individual nematode. Average velocity over a certain length of the track was measured by obtaining the total length traveled by the centroid of a nematode between a certain number of image frames (minimum 7) taken at one-second time intervals. This distance is then divided by the total number of frames between the beginning and ending worm positions to obtain an average velocity in  $\mu\text{m sec}^{-1}$ . This data analysis is done by PERL script language. Comparison is made between the average velocity calculated manually and the average velocity extracted by the PERL script. There was consistency between the two methods of data calculation.

Combined with the computer-aided image tracking software, we attempted to make this technique of experimentation, data recording, and analysis as automated and reliable as possible with the available technology.



### 3.2.7 Experimental Results

Figure 3.5 shows a comparison of the velocity of the two isolates of *O. dentatum* nematode (SENS and LEVR) when passing through different fixed sine-wave channels, each with a different wavelength and a fixed amplitude of 120  $\mu\text{m}$ .

The velocity measurements show a peak at the center where the wavelength of the sine-wave channel closely matches the natural wavelength of the nematode. At both lower side and higher side of the wavelength axis, the velocity shows a clear drop. For the SENS isolate, we noticed that the velocity data point at 396  $\mu\text{m}$  is similar to its velocity at 330  $\mu\text{m}$ , while we noticed a significant difference for LEVR at these two data points. The LEVR velocity is much faster in the  $\lambda = 396 \mu\text{m}$  channel than in the  $\lambda = 330 \mu\text{m}$  channel.

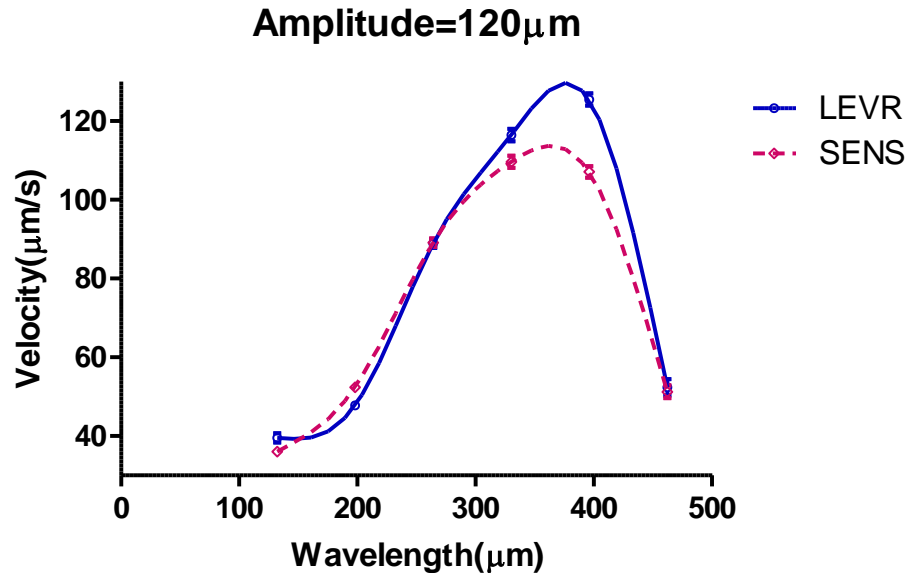


**Figure 3.5:** The velocity plots of the two different isolates of *O. dentatum* nematode (SENS and LEVR) in fixed sine-wave channels having different wavelengths. The x axis denotes the wavelength. The amplitude of the channel is fixed at 120  $\mu\text{m}$ .

Referring to the wavelength measurement reported in Chapter 2, we noticed that LEVR is measured to have a higher wavelength than SENS (SENS  $372.9 \pm 7.1 \mu\text{m}$  (mean,  $\pm$  s. e.,  $n = 32$ ) and LEVR  $393.1 \pm 4.6 \mu\text{m}$  (mean,  $\pm$  s. e.,  $n = 35$ )). This confirms our previous hypothesis that the nematode will move faster when the channel parameters are most closely resembled its their natural locomotion parameter. In our case, the channel width  $\lambda = 396 \mu\text{m}$  closely matches the reported LEVR wavelength.

This initial result indicates a potentially fast and automated method of distinguishing two different isolates of a sample parasitic nematode species. By testing the worms' responses to two custom-made sine-wave channels and comparing their responses by measuring their average velocity, we would be able to distinguish one isolate from the other one. With the help of image tracking and analysis software, this proposed testing method can be carried out automatically and relatively fast compared to manual calculations.

The velocity results of the isolates (SENS and LEVR) in other two sets of microfluidic devices (at fixed amplitude ( $A = 60 \mu\text{m}$  and  $A = 240 \mu\text{m}$ )) are also shown in Figures 3.6 and 3.7. We notice that there is a clear reduction of velocity in sine-wave trenches having these two amplitudes. This is due to the fact that these amplitudes are not close to the natural amplitude of the worm. This increases the challenge posed to the worms to move forward, thereby slowing down their measured velocity. No significant difference is observed between SENS and LEVR isolates since the amplitudes of the sine-wave trenches are far from the natural parameters which hide any underlying differences observed earlier in Figure 3.5. One interesting observation from Figures 3.6 and 3.7 is that there are two distinct peaks in the velocity plots for both isolates at the sine-wave amplitude of  $60 \mu\text{m}$ . One

possible explanation is that, at each peak, the  $A/\lambda$  ratio of the sine-wave channel matches the natural  $A/\lambda$  ratio of the worms [23]. At the peak, both the amplitude and wavelength are almost halved at these two data points.

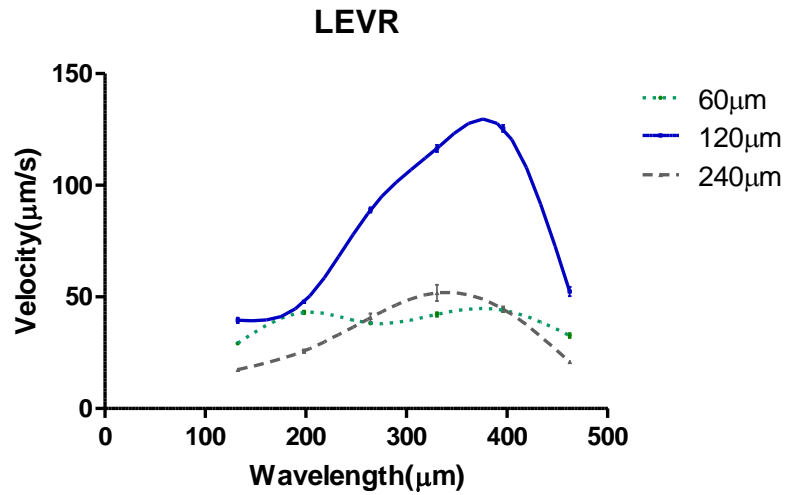


**Figure 3.6:** Velocity plots for the LEVR isolate in sine-wave channels. The x axis denotes the wavelength. The amplitude of the channel here is 60 μm, 120 μm and 240 μm.

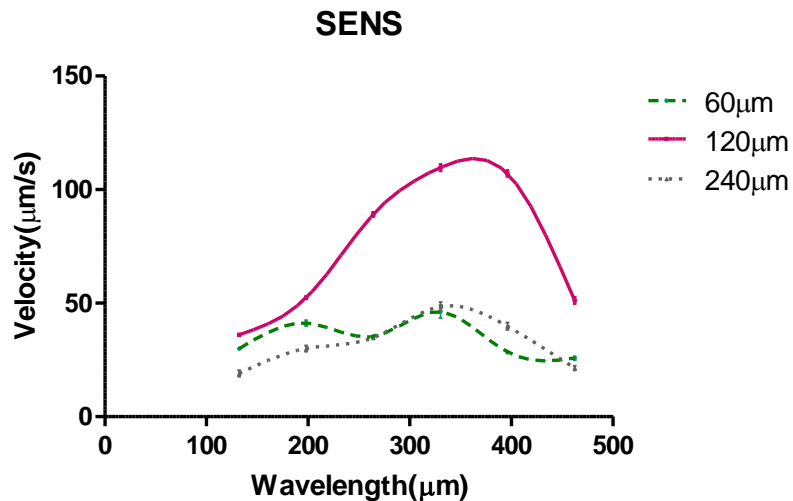


**Figure 3.7:** The velocity plots for the SENS isolate in sine-wave channels. The x axis is the wavelength. The amplitudes of the channels are 60 μm, 120 μm and 240 μm respectively.

### 3.3 Frequency Modulated (FM) Sine-wave Channels

#### 3.3.1 FM Channel Designs

The previous sinusoidal wave channels with various combinations of wavelengths and amplitudes (design 1 and 2) provide a good approach to investigate the nematode response in a predefined sine-wave confinement. The limitation of the design is that prior knowledge of device dimensions is needed and the number of devices being tested is unrealistic for testing multiple isolates or species. However, in an actual worm sorting application, we may not often have knowledge about the nematode's locomotion parameters which may alter with age or environmental factors (e.g. temperature, drugs). An ideal worm sorter should be able to identify and differentiate various known and unknown strains in a minimum number of trials.

Our previously discussed sine-wave designs could be improved by designing sine-wave channels with a continuously changing amplitude and wavelength parameters. In the field of electronic communication theory, this is called amplitude modulation (AM) or frequency modulation (FM) where the amplitude or wavelength of the sine-wave channel is 'chirped' or modulated. In an analogous manner, we borrow these acronyms here to describe the new worm sorting devices. This method allows us to investigate the nematode response with different locomotion parameters without prior knowledge about these parameters. One huge advantage of the proposed modulated channels is an *off-the-shelf* sinusoidal wave channel could be used to test various types of isolates. This provides ease of mass production, lower cost, faster screening and attractiveness as a disposable chip for field applications.

Furthermore, there is an additional possibility of collecting more information about the mechanical strength of isolates from these measurements. Currently, mechanical force sensors are used to measure the contractile forces of nematodes but are limited to large nematodes. In our devices, for example, we would be able to indirectly measure the force applied by the nematode to push forward. Our previous work has shown that this tangential force is related to the ratio of worm's amplitude to wavelength. Both AM and FM channels would challenge the worm to conform its body to the channel dimensions and to push against the channel sidewalls to move forward. This challenge would keep rising as the modulation is increased along a single device. Eventually, the worm would reach a certain section of the device beyond which it fails to move forward. Here the worm would either stop or retract. This cut-off point or range would be identified for each nematode isolate and the information subsequently used to differentiate isolates in a mixed population. We now demonstrate this simple approach of sorting worm isolates. Figure 3.8 shows two examples of AM and FM channels.

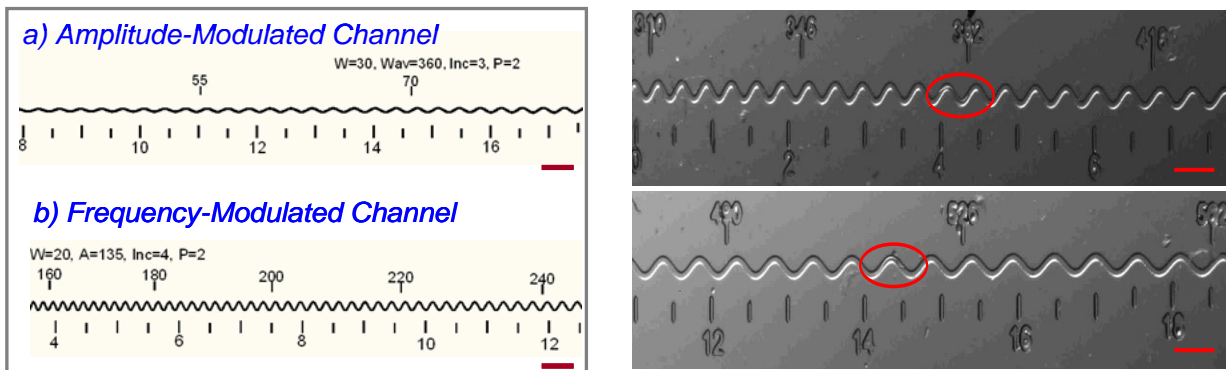


**Figure 3.8:** The two types of modulated channels: amplitude modulation and frequency modulation. The AM and FM masks are shown on left while snapshots of single worms in a section of FM channel is shown on right.

The Equation (3.1) shows an expression for a frequency modulated sine wave channel. If the wavelength  $\lambda$  varies linearly with the  $x$  coordinate in a channel aligned in the  $x$  axis, the  $y$  coordinate is calculated to be  $y(x) = A \sin(2\pi x/(\lambda_0 + c_1 x))$ , where  $\lambda_0$  and  $c_1$  are all constant coefficient and  $A$  is the amplitude of the sinusoidal wave.

$$\lambda(x) = \lambda_0 + c_1 x$$

$$y(x) = A \sin\left(\frac{2\pi x}{\lambda(x)}\right) = A \sin\left(\frac{2\pi x}{\lambda_0 + c_1 x}\right) \quad \text{Equation (3.1)}$$

The FM sinusoidal wave channels are designed to have the wavelength variation in the range from 10  $\mu\text{m}$ -718  $\mu\text{m}$ . The amplitude of the sine-wave is set fixed at 135  $\mu\text{m}$  which closely matches *O. dentatum*'s natural wavelength. The width of the channel is set at 30  $\mu\text{m}$ . To ensure smooth entrance of the worms into the channel from the input port, the initial section the microfluidic chip is designed to have a wavelength similar to the nematode's natural wavelength. One input/output port is shared by multiple (three) channels to increase the throughput and efficiency. A total of four input/out port ports are included in a single chip. The entire channel is 3 to 4 cm long.

### 3.3.2 Device Fabrication

The experimental setup and fabrication are similar to that discussed in Section 3.2. Figure 3.9 shows a microphotograph of FM sine-wave chip used in an experiment.

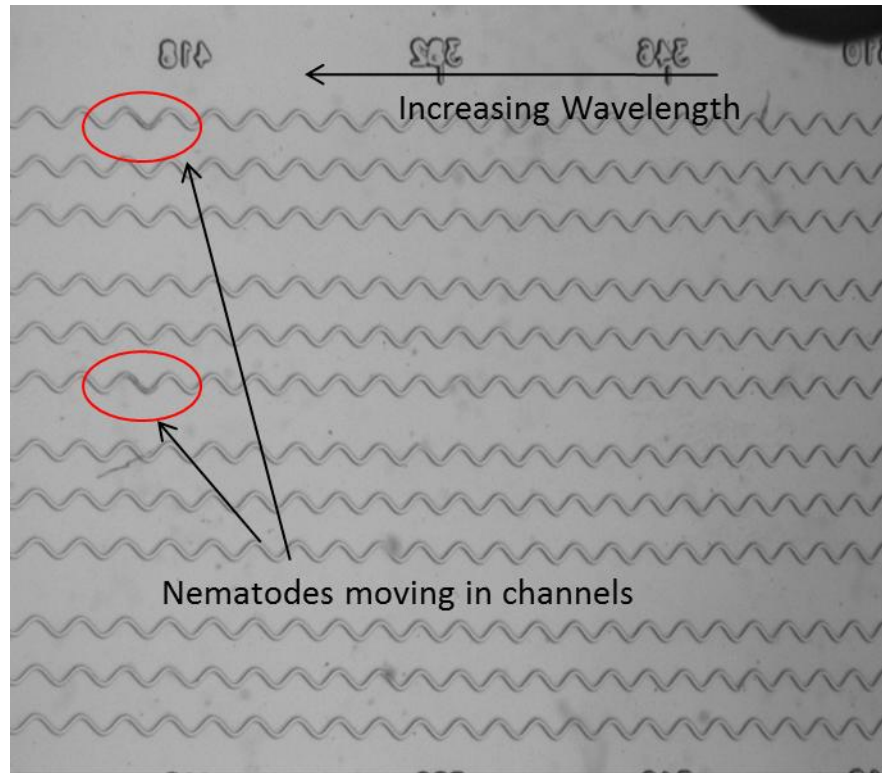


**Figure 3.9:** Fabricated FM sine-wave channels. On the left side of the channel, the wavelength is  $424 \mu\text{m}$  and on the right side wavelength is at  $310 \mu\text{m}$ . The wavelength gradually changes from one side to the other side. Three channels shares one input/output port (not shown in figure) to make fully utilization of the area and total 12 channels are packed in one device to increase the throughput.

### 3.3.3 Extraction of Locomotion Parameters

**Average Instantaneous Velocity:** The nematodes with regulated forward movement exhibit a gradually changing velocity over varying wavelength along a FM device. A worm's instantaneous velocity is defined as centroid position difference traveled by the worm's centroid over a short time period ( $<10 \text{ sec}$ ). In our experiments, the videos are analyzed using the custom tracking software written using C++ which generates a .csv file with centroid position data along time for each worm track. The video is taken at the speed of 1 frame per second. Each instantaneous velocity data is calculated and associated with its

current position. The position is linked to a corresponding wavelength and amplitude. These velocity data are grouped section-wise according to the designed wavelength or amplitude on the chip. This post data analysis procedure is completed by PERL script program.

**Cut-off Region:** The nematodes face gradually increasing challenge along the FM sine-wave channels before they eventually fail to respond. These are regions where the nematode cannot pass through [25]. We call these sections as cut-off regions defined as locations where the nematodes are able to reach but unable to cross. These regions can be easily identified by a visual check. The continuously modulated sinusoidal channels provide us this unique benefit that is relatively difficult and time-consuming to test in the fixed wavelength or amplitude channels.

**Turns and Stops:** During the experiment, we noticed that, as the channel challenge increases, the velocity decreases and so do other locomotion parameters that carry information about the worms' struggle in forward movement. One noticeable effect is as the amplitude increases, the movement of the nematode occurs with frequent stops. The number of turns and stops is apparently higher in more challenging sections of the AM or FM devices. The turns and stops are grouped for every section according to the predefined sets of trench wavelengths and amplitudes. Later, we normalize these data by dividing using the number of frames they travelled to make a fair comparison between the different experimental runs.

### 3.3.4 Experimental Results

We tested two isolates of *O. dentatum*: LEVR and SENS. The average velocity shows high value at wavelengths which match the nematodes' natural wavelength, as shown in Figure 3.10. As the FM trench wavelength shifts either side of this peak, the velocity



gradually drops. We noticed that, in most outer sections, the SENS has a lower velocity than LEVR. The SENS has a peak at a smaller wavelength than the LEVR. This is consistent with the result reported in Chapter 2 where the SENS has a smaller wavelength than LEVR.

Comparing individual responses of the isolates, we noticed that the LEVR is able to adapt better than SENS at FM sections of extreme wavelengths. The velocity changes are more gradual for LEVR compared to that for SENS. One possible explanation could be that the LEVR isolates not only acquire a higher resistant to the drug levamisole but also improve themselves in other facets such as adaptability. This is also confirmed in experimental results discussed later.

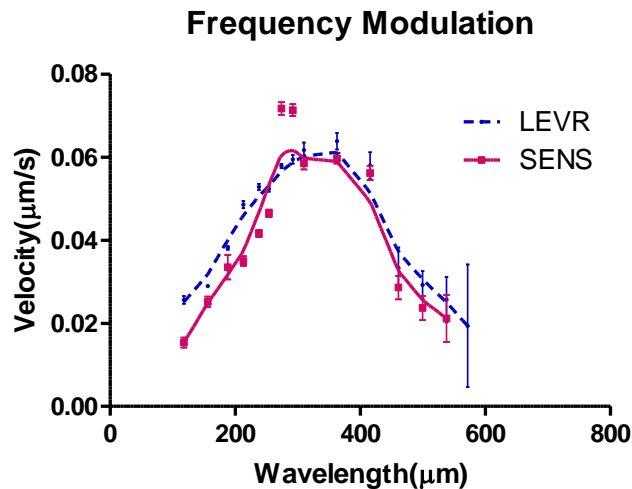


**Figure 3.10:** The average instantaneous velocity with respect to the wavelength is shown for SENS and LEVR *O. dentatum* larvae. The velocity shows a peak when the channel wavelength closely matches the worms' natural wavelength and reduces gradually when the wavelengths shift to either side. The amplitude of the channel is fixed at 135 µm which is selected to match the nematodes' natural parameter. We observe a peak in the SENS velocity at around 330 µm while the LEVR shows a peak at a slightly longer wavelength. We also notice the LEVR velocity is generally higher than SENS at regions far off from the center wavelength.

The turn probability LEVR and SENS along the wavelength axis are shown in Figure 3.11. They are post-processed using PERL script after the position data is produced by the custom-developed image tracking software. The turn probability shows a valley with gradually changing channel wavelength. When the channel's wavelength closely matches the natural amplitude, the turn probability shows a dip. As wavelength increases, both SENS and LEVR tend to change the direction of forward movement more often, which represents an increase in the turn probability. There is no significant difference observed between SENS and LEVR isolates in most sections.

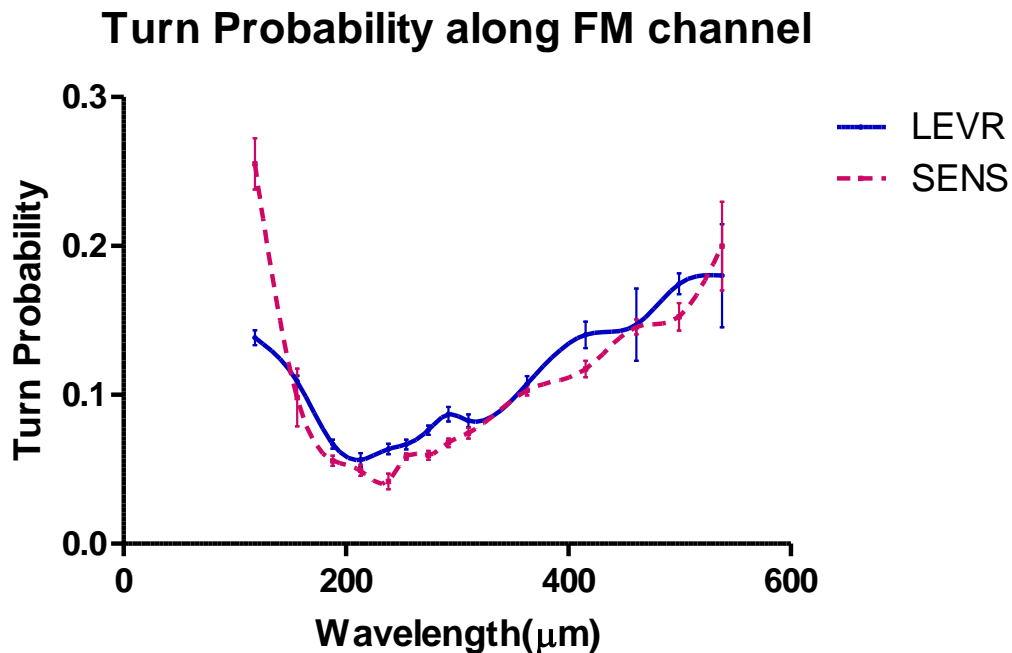


**Figure 3.11:** The measured turn probability with respect to the wavelength is shown for SENS and LEVR *O. dentatum* larvae. The turn probability shows a valley where the trench wavelength is similar to the natural wavelength and gradually increases as the trench wavelength shifts to either side. The amplitude of the FM channel is at 135  $\mu\text{m}$ . There is no significant difference in wavelength between SENS and LEVR larvae at most intermediate sections.

The stop probabilities for LEVR and SENS are plotted in Figure 3.12. The stop probability shows a valley in the middle of the wavelength axis and a steep increase at either extreme wavelength value. When the channel's wavelength closely matches the nematode's inherent wavelength, the worms tend to move freely and show less resistance in the movement. As wavelength challenge increases, both SENS and LEVR tend to make more frequent stops and show an increase in the stop probability.

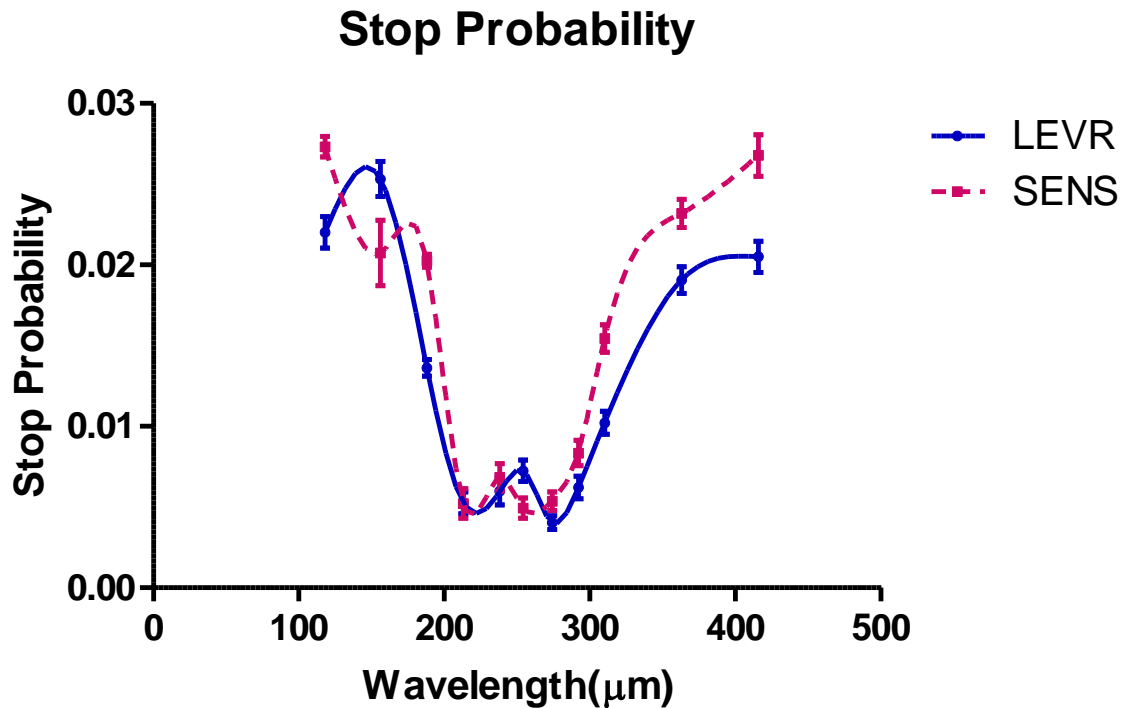


**Figure 3.12:** The measured stop probability with respect to the wavelength is shown for SENS and LEVR *O. dentatum* larvae. The stop probability shows a dip when the channel wavelength is similar to the worm's natural wavelength and increases when the wavelengths are at high or low end. The amplitude of the FM channel is at 135 μm. There is no significant difference between SENS and LEVR larvae at most sections. Interestingly we see a clear increase of the stopping probability for SENS at a high wavelength of around 420 μm. This corresponds to the fact that SENS has a shorter wavelength than the LEVR and is unable to adapt as well as the LEVR isolate.

The cut-off region is also reported in Figure 3.13. The SENS shows a cut-off region of 565-580  $\mu\text{m}$  and LEVR has a cut-off region of 565-580  $\mu\text{m}$  in the FM device. With 3  $\mu\text{M}$  levamisole drug solution, the levamisole-sensitive SENS has a large drop in their cut-off points while not much difference is observed for levamisole-resistant LEVR isolate.

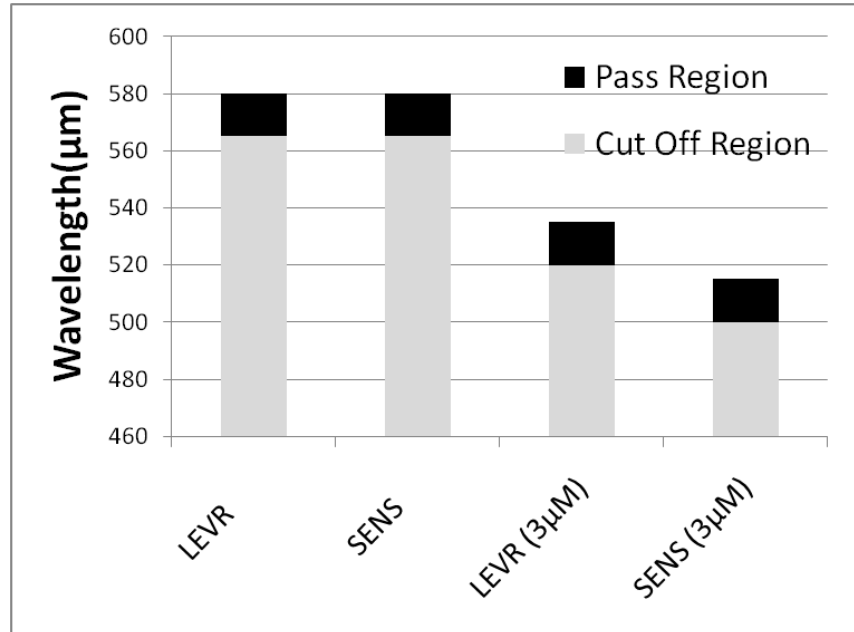


**Figure 3.13:** The cut-off region of the wavelength is shown for SENS and LEVR *O. dentatum* larvae. The cut-off region for both SENS and LEVR drops where 3  $\mu\text{M}$  levamisole drug applied, but the SENS has a much more significant drop. This coincides with the fact that SENS is more sensitive and tends to lose more vigor when exposed to drug.

### 3.4 Amplitude Modulated (AM) Sine-wave Channels

#### 3.4.1 AM Channel Designs

Similar to the FM channels, amplitude modulated (AM) sine-wave channels are designed to investigate the response of nematodes to challenges of increasing or decreasing trench amplitude. In these AM channels, the amplitude of the sine-wave is gradually changing from one side to the other side of the channel. Based on the nematodes' natural

amplitude, it is expected that nematodes will have reduced velocity along the channel and eventually fails to proceed forward beyond a certain section.

Equation (3.2) shows an expression for an amplitude modulated sine wave channel. If the amplitude  $A$  varies linearly with the  $x$  coordinate in a channel aligned in the  $x$  axis, the  $y$  coordinate is calculated to be  $y(x) = (A_0 + c_2x) \sin\left(\frac{2\pi x}{\lambda}\right)$  where  $A_0$  and  $c_2$  are all constant coefficients and  $\lambda$  is the wavelength of the sinusoidal wave.

$$y = A(x) \sin\left(\frac{2\pi x}{\lambda}\right) = (A_0 + c_2x) \sin\left(\frac{2\pi x}{\lambda}\right) \quad \text{Equation (3.2)}$$

The AM sinusoidal channel is designed to have the amplitude changing from 10  $\mu\text{m}$  to 399  $\mu\text{m}$ . The wavelength of the sine-wave is set to 360  $\mu\text{m}$ , which close matches the nematode's natural wavelength. Similar to FM channel, the microfluidic chip is designed here to have an input section starting at the nematode's natural amplitude to allow smooth entrance of worms into the channel. One input/output port is shared by multiple (three) channels to increase the experiment throughput and efficiency. A total of four input/output ports are accommodated in a single chip. The width of the channel is set at 30  $\mu\text{m}$ . The number of the channels per device is limited by the mask design rule which is directly related to the fabrication process. A higher channel density could be realized in a well-controlled fabrication process and can be benefited from advanced soft lithography process, i.e. high resolution of mask, improved aspect ratio of SU-8 mask.

### 3.4.2 Device Fabrication, Experimental Protocols and Data Analysis

The experiment, fabrication and data analysis are similar to Section 3.3. Average instantaneous velocity, turn probability and stop probability are extracted and reported.

Figure 3.14 shows a micro photograph of an AM sine-wave chip taken in one experiment. The worms enter into the channels at a wavelength of  $135\ \mu\text{m}$  and face increasing challenge with increasing amplitude as they move forward along the channel. Markers and rulers are designed for calibration purpose.

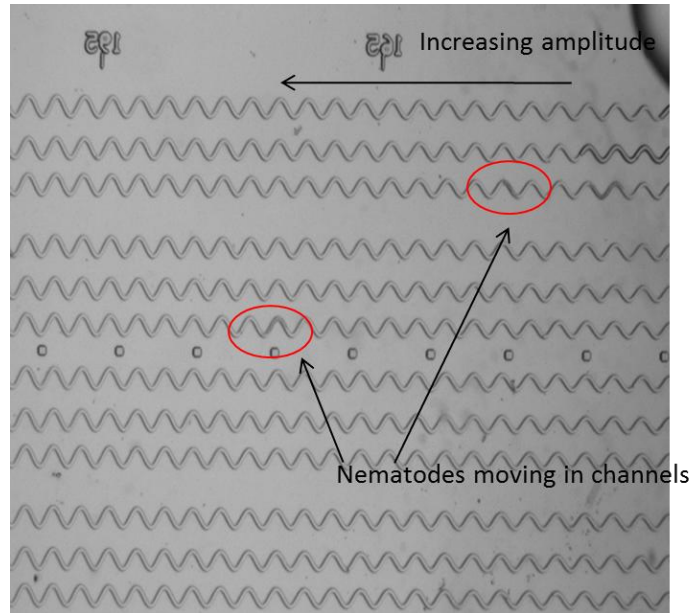


**Figure 3.14:** Amplitude modulated sinusoidal wave channels. On the left side of the channel, the amplitude is around  $198\ \mu\text{m}$  and on the right side amplitude is at  $135\ \mu\text{m}$ . The amplitude changes gradually in between these two extremes. Three channels share one input/output port (not shown in figure) to make fully utilization of the area and increase throughput. Markers was added for calibration purpose

### 3.4.3 Experimental Results

We tested the two isolates of *O. dentatum* LEVR and SENS. Their average instantaneous velocities are analyzed using the developed imaging tracking software and post processed using PERL script. The velocity is gradually changing along the amplitude axis. Both LEVR and SENS show a peak velocity in the amplitude region between  $160\text{-}220\ \mu\text{m}$ . These regions are close to their inherent amplitude. As amplitude challenge increases, both

SENS and LEVR isolates show a drop in the average velocity. We notice the SENS isolate has a velocity generally lower than LEVR at the extreme regions. The curves are plotted in Figure 3.15. The difference in their response verifies our previous conclusion for FM channels: the LEVR isolate is more active and adaptable than SENS.

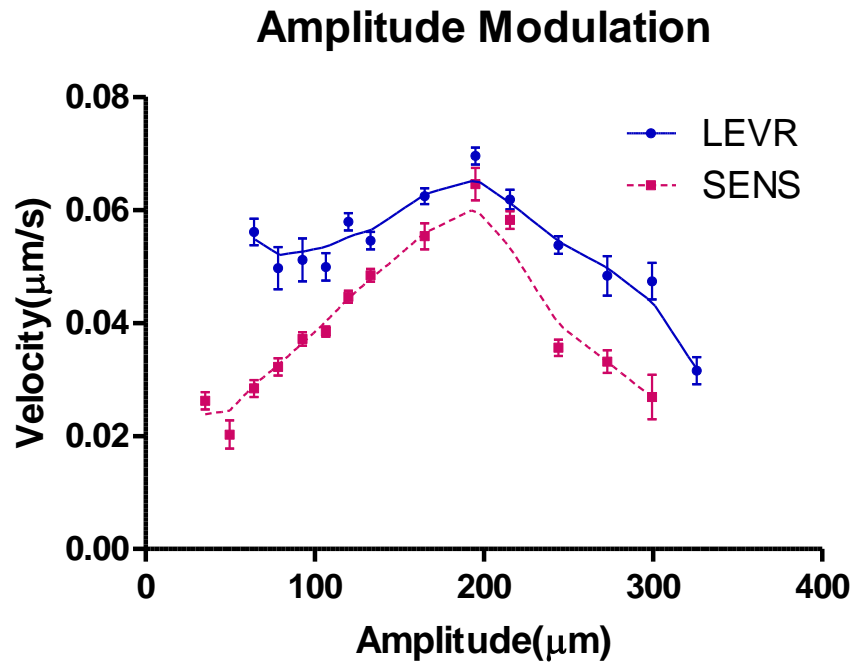


**Figure 3.15:** The measured average instantaneous velocity with respect to the amplitude for SENS and LEVR *O. dentatum* larvae. The velocity curves exhibit a peak when the trench wavelength is similar to the natural amplitude and drops when the amplitude is at extreme values. The wavelength of the channel is set at 360 μm. As the trench amplitude increases or decreases away from the peak value, the velocity of SENS reduces significantly more than LEVR isolates.

The turn probability LEVR and SENS are plotted in Figure 3.16. They are post-processed using PERL script after the position data is generated by the image tracking software. The turning probability shows a valley in the center. When the channel amplitude

closely matches the natural amplitude of the nematode, the turning probability shows a low plateau region. As amplitude challenge increases, both SENS and LEVR tend to change their moving direction more often and this increases the turn probability. We noticed that the dip of SENS worm is apparently at a higher position than the LEVR. This corresponds to the result reported in Chapter 2 where the SENS isolate has a higher amplitude. Although their velocity curve does not clearly reflect the difference in worms' natural amplitude, it is worth mentioning that the plots of their turning probabilities clearly show a difference.

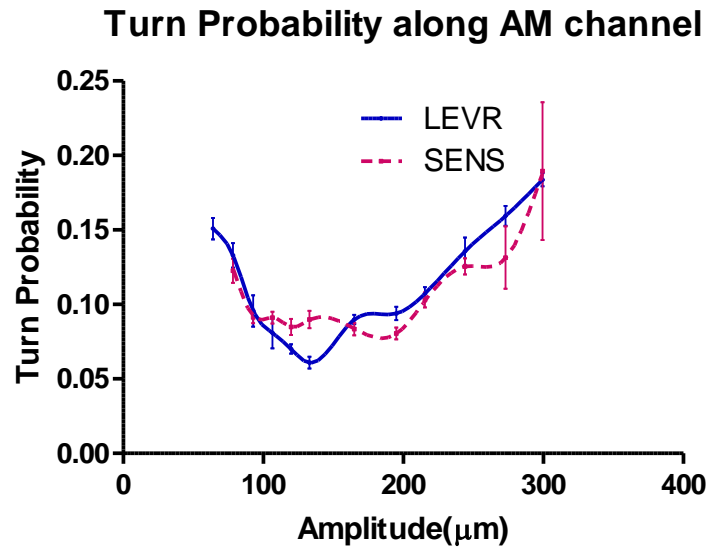


**Figure 3.16:** The measured turn probability with respect to the amplitude is plotted for *O. dentatum* SENS and LEVR larvae. The wavelength of the channel is at 360 μm. There is no significant difference in turn probability between SENS and LEVR larvae at most channel sections. The position of the valley for SENS is apparently higher than LEVR.

The stop probabilities for LEVR and SENS are plotted in Figure 3.17. The stop probability shows a similar shape as Figure 3.16: a low flat in the central part of the amplitude axis and a steep increase at extreme amplitudes. When the channel's amplitude closely matches the natural amplitude of the isolates, the nematodes tend to move freely and



make fewer stops. As amplitude challenge increases, both SENS and LEVR tend to make more frequent stops, showing an increase in the stop probability.

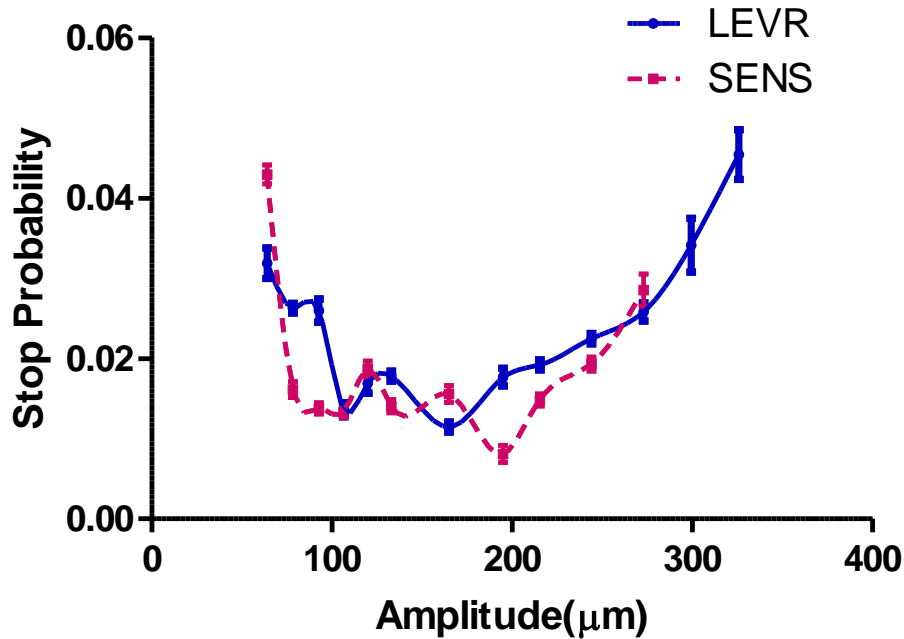


**Figure 3.17:** The measured stop probability with respect to the amplitude is shown for SENS and LEVR *O. dentatum* larvae. The stop probability shows a dip when the channel amplitude is similar to the worm's natural amplitude and steadily increases when the amplitude is at extreme values. The wavelength of the channel is at 360 μm. There is no significant difference between SENS and LEVR larvae at most data sections. However, similar to the turn probability case, we also observed the curve dips for SENS and LEVR happen at different points. The valley for SENS happens at apparently higher positions than LEVR. This is possibly because the SENS is reported to have larger amplitude than the LEVR [22].

The cut-off region is plotted in Figure 3.18. The SENS isolates shows a cut-off region at the channel amplitude of 310-325 μm while the LEVR nematode has a cut-off region at the channel amplitude of 350-365 μm. Although SENS has a larger amplitude, as reported in [22], the cut-off point observed is lower than LEVR. This reflects the LEVR isolate has a

stronger ability to exploring surroundings and a stronger adaptability. Upon exposure to 3  $\mu\text{M}$  levamisole, SENS has a large drop in its cut-off point while there is no significant drop for the LEVR isolate.

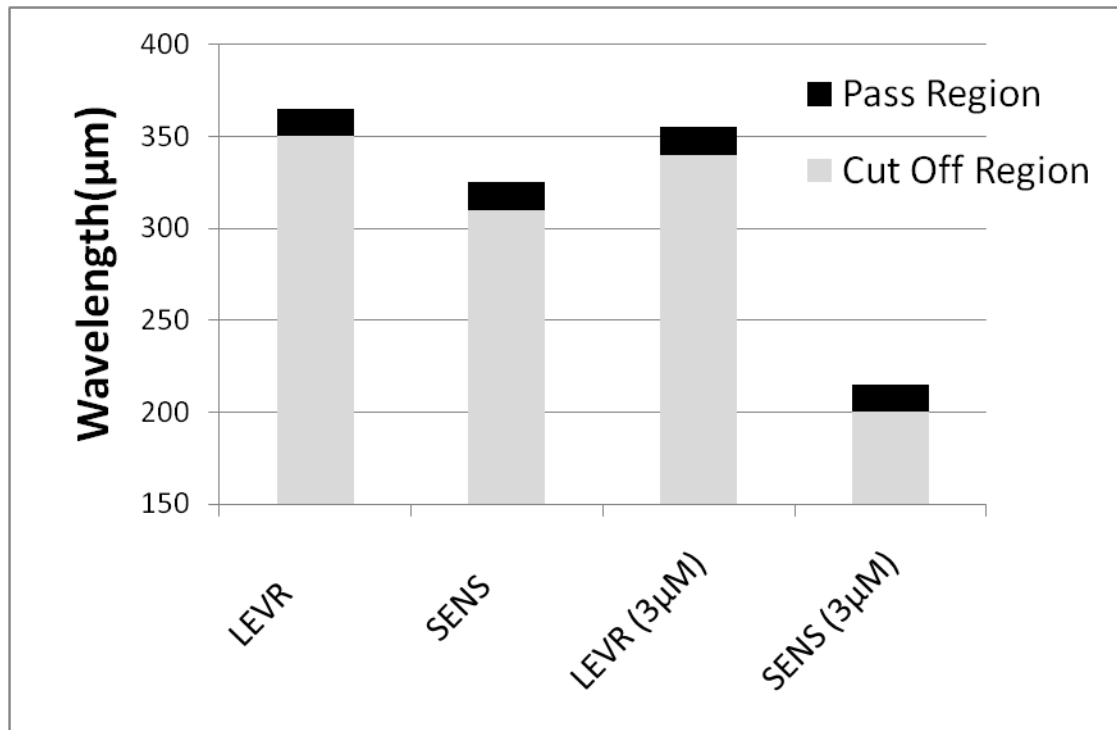


**Figure 3.18:** The cut-off region in AM device is shown for SENS and LEVR *O. dentatum* larvae. The cut-off region (for both SENS and LEVR) drops upon exposure to 3 $\mu\text{M}$  levamisole a, but the drop is significant for SENS. This shows the higher levamisole resistance of LEVR isolate compared to the SENS isolate.

### 3.5 Discussion

In this chapter we presented a microfluidic method of differentiating two strains of a sample nematode species. For this, we used multiple sets of frequency-modulated and amplitude-modulated sine-wave channels to characterize nematode response with defined

locomotion parameters. Instead of passively extracting the nematodes' locomotion parameters from biological experiments, we allow the worms to challenge themselves through these passive devices and demonstrate differences in locomotion parameters. We showed that the locomotion behavior is different for the two nematode isolates tested: SENS and LEVR of *O. dentatum* larvae. We are the first group to propose such a modulated sinusoidal wave channel device as an automated worm sorter. We confirmed that the LEVR isolate is better adapted to these devices compared to the SENS isolate. This valuable information gathered from the conducted experiments was used to distinguish the SENS from the LEVR isolate.

The sine-wave microfluidic channels provide a new and easy way for detection of drug resistance in other strains and possible application for reverse genetic experiments. The real-time monitoring of worm adaptability in AM/FM wave channels is attractive because of the ability to screen and sort worms based on differences in their adaptability and inherent mechanical strength. This is in contrast to manually measuring locomotion parameters of nematodes in straight channels which is tedious and with low throughput. The AM/FM channels do not require prior knowledge of worm physiology or locomotion parameters. An *off-the-shelf* AM/FM channel can be used to test different known or unknown species of parasitic nematodes in a mixed population. This is particularly appealing for field applications where nematodes of mixed phenotype and genotype can be found. In addition, our design allows us to run multiples of experiments (each in an individual channel) simultaneously and record the nematode movement simultaneously from all the channels.

This research work on AM/FM devices has been successfully demonstrated on other nematode species such as *C. elegans* by our group.

## Chapter 4

### Conclusions and Future Scope

We reported a novel charge-sensing platform using an extended floating-gate device (UGFET) that is scalable and fully compatible with standard CMOS process. Simulation results based on finite element analysis predicted a high sensitivity: 150 pC of charge per  $\text{mm}^2$  on the sensing area produces  $\sim 1\text{V}$  change in the floating-gate voltage. We fabricated the UGFET charge sensor. The UGFET transconductance and subthreshold measurements verified that the UGFETs show markedly different responses with polyelectrolytes and poly amino acids of varying polarity and concentration. This neuromorphic sensing method is nondestructive, repeatable, reusable, and easily refreshed. Since most biological species (single cells, proteins, DNA) have intrinsic charge, UGFET charge-modulated microarrays could serve as fast, portable, and inexpensive alternatives for biochemical sensing applications.

We presented a worm motility device for measuring phenotypic variations and drug dose response across nematode isolates and species with increased throughput and sensitivity. We identified significant differences in morphological parameters (i.e. wavelength, amplitude, tangential force) and locomotion parameters (i.e. oscillation frequency, average forward velocity, and track signatures) among the different groups of nematodes studied. An automated image tracking program is developed as a faster way to analyze data and extract track signatures that correlate to the resistance levels of individual isolates. Our method of identifying differences in worm parameters could possibly provide a means of sorting a mixed worm population with improved sensitivity and throughput.

Lastly, we reported a new bioassay as a worm sorter. We designed and fabricated frequency and amplitude modulated sine-wave channels and applied it to automatically screening drug resistance of nematodes. We were able to observe changes in worm locomotion using a predefined set of parameters. Our experiments show that the two isolates have different locomotion phenotypes in the sinusoidal wave channels. The technique reported here would lead to the development of a simple, flexible, and robust platform to conduct high-throughput drug screening on parasitic nematodes.

## References

1. Dzyadevych, S.V, Soldatkin, A.P., El'skaya, A.V., Martelet, C., Renault, N., "Enzyme biosensors based on ion-selective field-effect transistors", *Anal. Chim. Acta.* 568: 248-258, 2006.
2. Wrobel, G., Seifert, R., Ingebrandt, S., Enderlein, J., Kaupp, U., Offenhausser, A., "Cell-Transistor Coupling: Investigation of Potassium Currents Recorded with p- and n-Channel FETs", *Biophys. J.* 89: 3628-3638, 2005.
3. Kim, D., Jeong, Y., Park, H., Shin, J., Choi, P., Lim, G., "An FET-type charge sensor for highly sensitive detection of DNA sequence", *Biosens. Bioelectron.* 20: 69-74, 2004.
4. Truman, P., Uhlmann, P., Stamm, M., "Monitoring liquid transport and chemical composition in lab on a chip systems using ion sensitive FET devices", *Lab Chip* 6: 1220-1228, 2006.
5. Barbaro, M., Bonfiglio, A., Raffo, L., "A Charge-Modulated FET for Detection of Biomolecular Processes: Conception, Modeling, and Simulation", *IEEE T. Electron Dev.* 53,1:158-166, 2006.
6. Shen, N., Liu, Z., Lee, C., Minch, B., Kan, E., "Charge-Based Chemical Sensors: A Neuromorphic Approach with Chemoreceptive Neuron MOS Transistors", *IEEE T. Electron Dev* 50, 10: 2171-2178, 2003.
7. Milgrew, M. J., Hammond, P.A., Cumming, D.R.S., "The development of scalable sensor arrays using standard CMOS technology", *Sensor Actuator B* 103: 37-42, 2004.
8. Patolsky, F., Timko, B., Yu, G., Fang, Y., Greytak, A., Zheng, G., Lieber, C., "Detection, Stimulation, and Inhibition of Neuronal Signals with High-density Nanowire Transistor Arrays", *Science* 313:1100-1104, 2006.

9. Georgiou P., Toumazou, C., “CMOS-based programmable gate ISFET”, *Electron. Lett.* 44 : 22, October 2008.
10. Bergveld, P., “Development, Operation, and Application of the Ion-Sensitive Field-Effect Transistor as a Tool for Electrophysiology”, *IEEE Trans. Biomed. Eng.* 19: 342, 1972.
11. Shen, N.Y., Liu, Z., Jacquot, B.C., Minch, B.A., Kan, E.C., “Integration of chemical sensing and electrowetting actuation on chemoreceptive neuron MOS (CvMOS) transistors”, *Sensor Actuat. B-Chem.* 102:35-43, 2003.
12. Kim, M., Shen, N.Y., Lee, C., Kan, E.C., “Fast and sensitive electret polymer characterization by extended floating gate MOSFET”, *IEEE T. Dielect. El. In.* 12:1082-87, Oct. 2005.
13. Tao, C., Chen, B., Pandey, S., “A novel floating gate biosensing device with controlled charge-modulation”, *IEEE/NIH Life Science Systems and Applications Workshop* , Washington, DC, 2007.
14. Chen, B., Tao, C., Pandey, S., “Fabrication and Characterization of a Novel Dual-Gate Charge-Sensing Device for Single Cell Studies”, *Material Research Society Spring Meeting* San Francisco, CA, 2008.
15. Pandey, S., Chen, B., Tao, C., “Novel Neuromorphic CMOS Device Array for Biochemical Charge Sensing”, *IEEE Engineering in Medicine and Biology Society Meeting*, Vancouver, Canada, 2008
16. Chen, B., Tao, C., Pandey, S., “Biochemical Sensing of Charged Polyelectrolytes with a CMOS Floating-gate Device Architecture”, *IEEE International Conference on Electro/Information Technology* 2008.



17. Kaplan, R.M., “Drug resistance in nematodes of veterinary importance: a status report”, *Trends Parasitol.* 20: 477-481, 2004
18. Albonico, M., Wright, V., Ramsan, M., Haji, H.J., Taylor, M., Savioli, L., Bickle, Q., “Development of the egg hatch assay for detection of anthelmintic resistance in human hookworms”, *Int. J. Parasitol.* 35: 803-811, 2005.
19. Diawara, A., Drake, L.J., Suswillo, R.R., Kihara, J., Bundy, D.A., “Assays to Detect beta-Tubulin Codon 200 Polymorphism in *Trichuristrichiura* and *Ascarislumbricoides*”, *PLoS Neglected Tropical Diseases* 3: e397, 2009
20. Martin, R.J., Bai, G., Clark, C.L., Robertson, A.L., “Methyridine (2-[2-methoxyethyl]-pyridine) and levamisole activate different ACh receptor subtypes in nematode parasites: a new lead for levamisole-resistance”, *Brit. J. Pharmacol.* 140: 1068–1076, 2003
21. Martin, R.J., “Modes of action of anthelmintic drugs”, *VET. J.* 154: 11-34, 1997
22. Chen, B., Deutmeyer, A., Carr, J., Robertson, A.P., Martin, R.J., Pandey, S., “Microfluidic bioassay to characterize parasitic nematode phenotype and anthelmintic resistance”, *Parasitol.*, doi:10.1017/S0031182010001010, available online July 2010
23. Gray, J. M., “Undulatory propulsion”, *Q. J. Microscop. Sci.* 94: 551–578, 1953
24. Gray, J. M., Lissmann, H.W., “The Locomotion of Nematodes”, *J. Exp. Biol.* 41: 135–154, 1964
25. Lockery, S.R., Lawton, K.J., Doll, J.C., Faumont, S., Coulthard, S.M., “Artificial dirt: Microfluidic substrates for nematode neurobiology and behavior”, *J. Neurophysio.* 99: 3136–3143, 2008
26. McNeal, R., “Locomotion. The Biology of Nematodes”, Taylor and Francis, London 345, 2002

27. Gray, J.M., Karow, D.S., Lu, H., Chang, A.J., Chang, J.S., Ellis, R.E., Marletta, M.A., Bargmann, C.I., “Oxygen sensation and social feeding mediated by a *C. elegans* guanylatecyclase homologue”, *Nature* 430: 317–322, 2004
28. Pierce-Shimomura, J.T., Morse, T.M., Lockery, S.R., “The fundamental role of pirouettes in *Caenorhabditiselegans* chemotaxis”, *J. Neurosci.* 19: 9557–9569, 1999
29. Ryu, W.S., Samuel, A.D., “Thermotaxis in *Caenorhabditiselegans* analyzed by measuring responses to defined thermal stimuli”, *J. Neurosci.* 22: 5727–5733, 2002.
30. Gray, J.M., Hill, J.J., Bargmann, C.I., “A circuit for navigation in *Caenorhabditiselegans*”, *Proc. Natl. Acad. Sci.* 102: 3184–3191, 2005
31. Hulme, S.E., Shevkopyas, S.S., Apfeld, J., Fontana, W., Whitesides, G.M., “A microfabricated array of clamps for immobilizing and imaging *C. elegans*”, *Lab Chip* 7: 1515–1523, 2007
32. Qin, J., Wheeler, A.R., “Maze exploration and learning in *C. elegans*”, *Lab Chip* 7: 186–192, 2007
33. Sia, S.K., Whitesides, G.M., “Microfluidic devices fabricated in poly(dimethylsiloxane) for biological studies”, *Electrophoresis* 24: 3563–3576, 2003.
34. Whitesides, G.M., “The origins and future of microfluidics”, *Nature* 442: 368–373, 2006.
35. Heng, X., Erickson, D., Baugh, L.R., Yaqoob, Z., Sternberg, P.W., Psaltis, D., Yang, C., “Optofluidic microscopy—a method for implementing a high resolution optical microscope on a chip”, *Lab Chip* 6: 1274–1276, 2006
36. Kerr, R., Lev-Ram, V., Baird, G., Vincent, P., Tsien, R.Y., Schafer, W.R., “Optical imaging of calcium transients in neurons and pharyngeal muscle of *C. elegans*”, *Neuron* 26: 583–594, 2000

37. Nagel, G., Brauner, M., Liewald, J.F., Adeishvili, N., Bamberg, E., Gottschalk, A., “Light activation of channelrhodopsin-2 in excitable cells of *Caenorhabditiselegans* triggers rapid behavioral responses”, *Curr. Biol.* 15: 2279–2284, 2005
38. Hu, S., Ren, X., Bachman, M., Sims, C.E., Li, G.P., Allbritton, N., “Surface modification of poly(dimethylsiloxane) microfluidic devices by ultraviolet polymer grafting”, *Anal. Chem.* 74: 4117–4123, 2002
39. Chronis, N., Zimmer, M., Bargmann, C.I., ”Microfluidics for in vivo imaging of neuronal and behavioral activity in *Caenorhabditiselegans*”, *Nat. Methods* 4: 727–731, 2007
40. Feng, Z., Cronin, C.J., Wittig, J.H., Sternberg, P.W., Schafer, W.R., “An imaging system for standardized quantitative analysis of *C. elegans* behavior”, *BMC Bioinformatics* 5: 115, 2004

## Appendix 1

### Image-tracking Software

In Chapter 3 our work utilizes an image tracking software for video analysis. This appendix gives a short description of our image tracking software. Figure A.1.1 shows a sample graphic user interface for the software and Figure A.1.2 shows a screenshot of a running video data analysis.

The worm tracking program runs the recorded videos through a number of steps to negate the background and extract worm motility parameters. Worm density and movement do not adversely affect the tracking system, though increased worm contact were seen to interrupt their tracking.

There are totally three steps in the video analysis process.

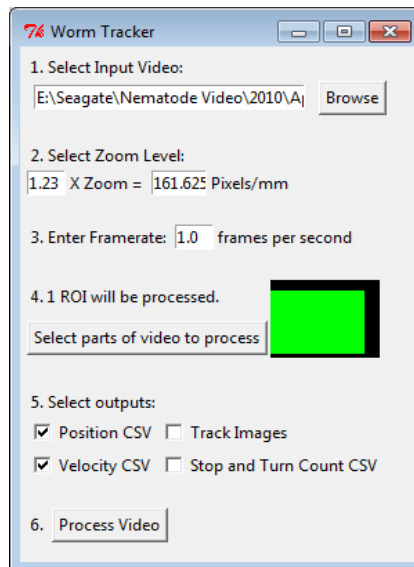
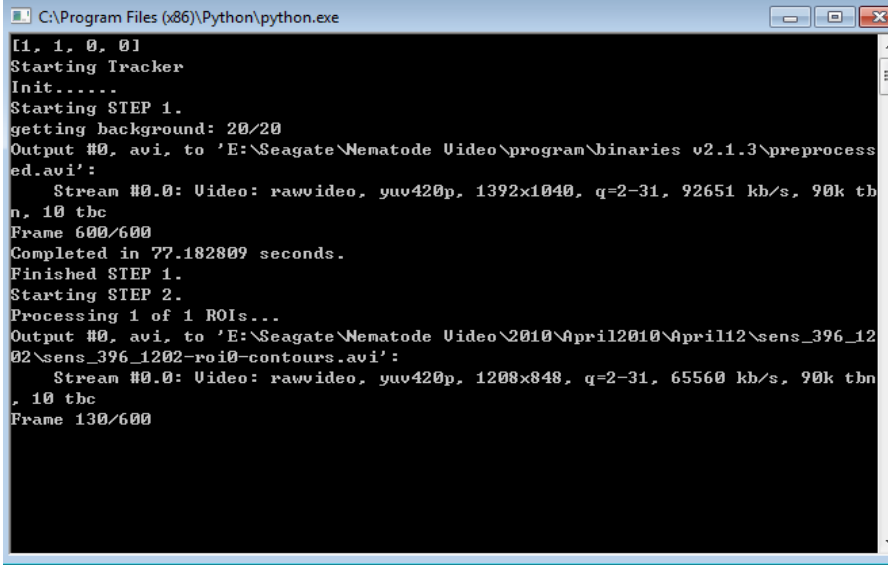


**Figure A1.1:** A sample graphic user interface for the image tracking software.



```

C:\Program Files (x86)\Python\python.exe
[1, 1, 0, 0]
Starting Tracker
Init.....
Starting STEP 1.
getting background: 20/20
Output #0, avi, to 'E:\Seagate\Nematode Video\program\binaries v2.1.3\preprocess
ed.avi':
  Stream #0.0: Video: rawvideo, yuv420p, 1392x1040, q=2-31, 92651 kb/s, 90k tbn, 10 tbc
Frame 600/600
Completed in 77.182809 seconds.
Finished STEP 1.
Starting STEP 2.
Processing 1 of 1 ROIs...
Output #0, avi, to 'E:\Seagate\Nematode Video\2010\April2010\April12\sens_396_12
02\sens_396_1202-roi0-contours.avi':
  Stream #0.0: Video: rawvideo, yuv420p, 1208x848, q=2-31, 65560 kb/s, 90k tbn, 10 tbc
Frame 130/600

```

**Figure A1.2:** A screenshot of a running video data analysis.

The first step is background negation. This step is used to negate the channel walls, other markings, and any particulates. It is able to identify the background in the presence of many worms by comparing a series of images over the duration of the input video. As the worms moving forward, they expose new parts of the background. For each successive image, areas that were lighter than previous frames were added to the background model. Combining a number of frames in this way produced a complete background model. The background is negated from the video and a threshold is applied. This produces an output video containing only white worms on an empty black background.

The Lucas-Kanade optical flow algorithm is used to compute motion vectors. Worm density and movement do not affect the tracking system. It only uses vectors that agree across the whole view, ignoring localized movements caused by worms. The algorithm generates motion vectors by tracking image features of the worm which may also have included particulates on the substrate or other unwanted patterns incorporated during channel

fabrication. To characterize motion in any direction, the program detects features in the image which have both sharp vertical and horizontal components. It also compensates for vibrations that occurred during the recording procedure by using the image-feature tracking technique.

In addition, the users are able to easily provide the program with information about specific regions of interest. This specifies the areas of the video that should be processed further, ignoring the rest. This allows the user to safely ignore irrelevant data, shorten execution time, and use separate sets of data from parallel experiments running in different channels.

The next step is worm segmentation and recognition. After background subtraction, polygons are fitted to the white shapes. Isolated regions such as particulates that do not have an interior area were eliminated, leaving only the channel boundaries. This step is used to improve performance and accuracy by safely ignoring erroneous data outside the channels and also to segregate data from multiple channels. Polygons that are too large or too small are discarded. This includes instances where two or more worms were in contact. Worm polygons were then matched between consecutive frames to provide tracking data over time. If no close match were found in the next frame, which may occur because of worm occlusion or worm contact, the track is terminated. If the same worm is recognized in later frames, a new track was started.

The last step is the extraction of motility parameters. The centroid of the worm at each frame is calculated as the centroid of the fitted polygon. The polygon is also used to calculate the bounding box to approximate the wavelength and amplitude. The posture of the

worm is represented by a series of segments running along its center. The program first tries to find a pair of points across the middle of the worm. The points are then alternately advanced (first in one direction and then the other) to minimize the distance between the points until they meet at the end of the worm. For each successive position of the points, the midpoint is added to the worm's spline. The spline points are then simplified to thirteen equally spaced points. We then extract the track signatures from the gathered data. These steps are shown in Figure A.1.3 respectively.

The program outputs a position data file in either csv or xls format which can be further analyzed by PERL scripts.

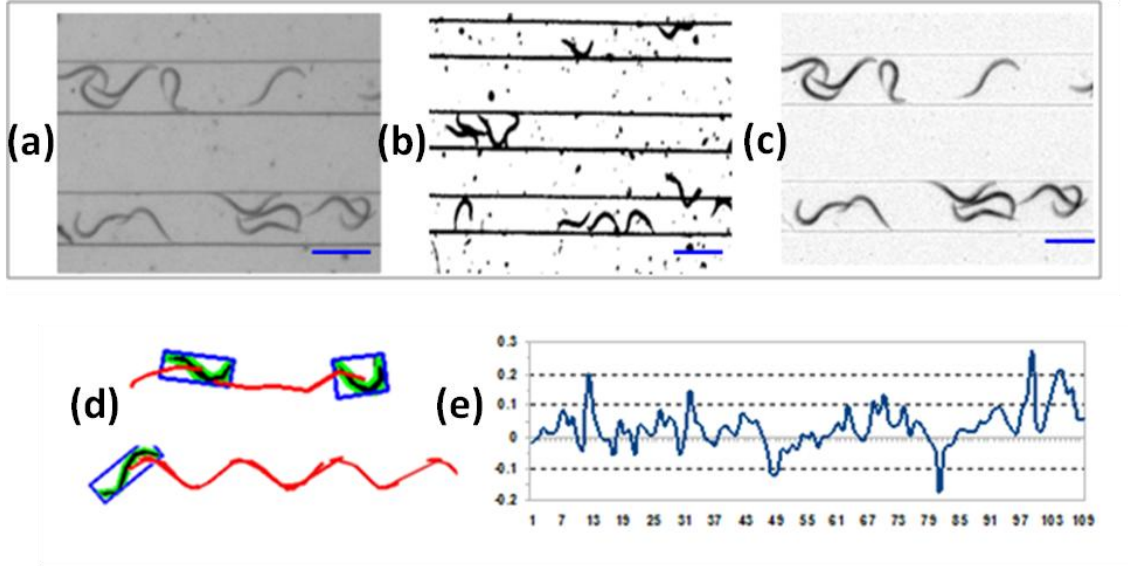


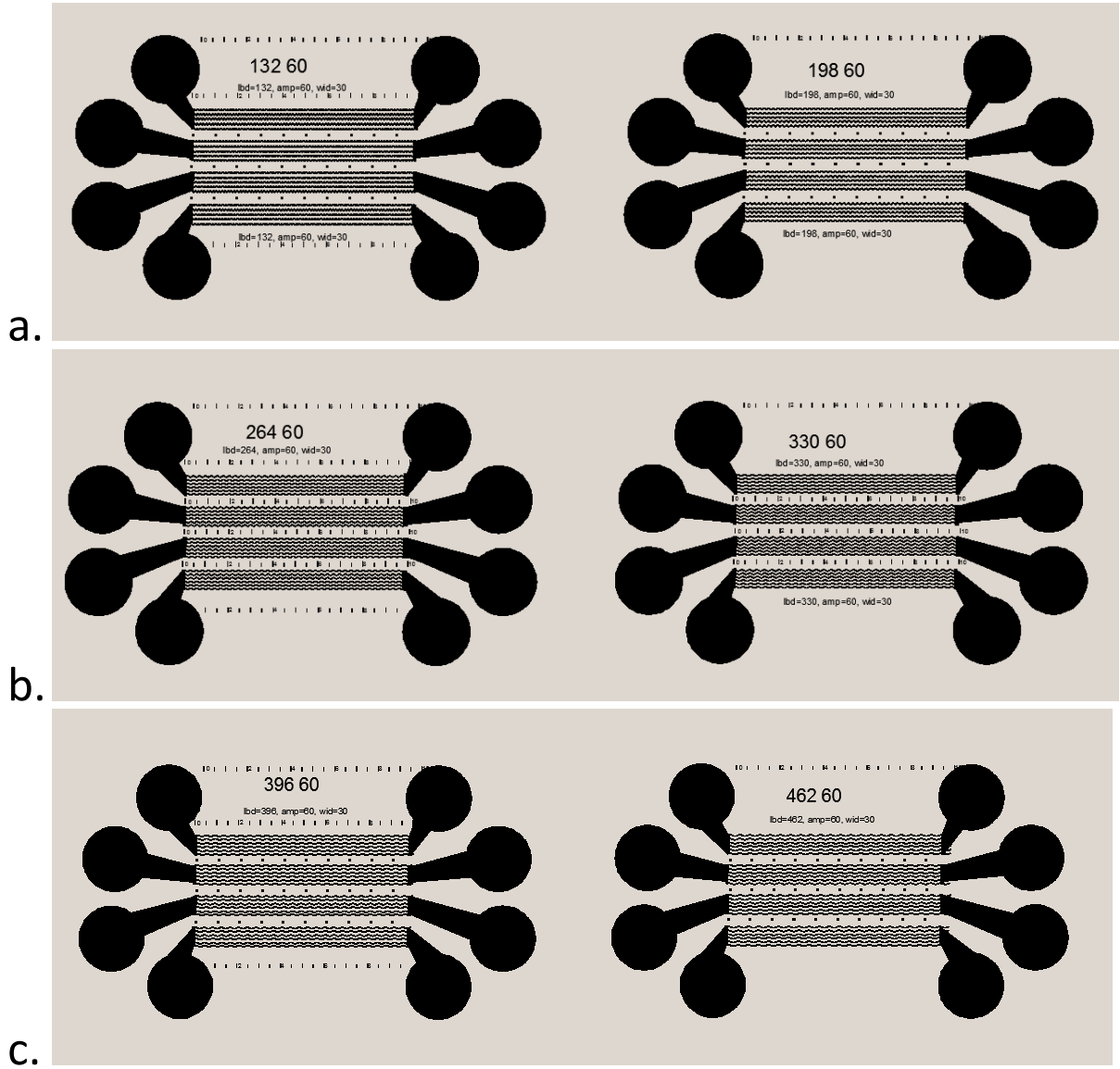
**Figure A1.3:** Three processing steps of the raw video from (a) to (b) shows background negation, from (b) to (c) shows segmentation and recognition and from (c) to (d) shows extraction of motility parameters. Using the image tracking software, the path of the worm is extracted out and the instantaneous velocity is calculated. (e) shows a sample instantaneous velocity profile of a nematode.

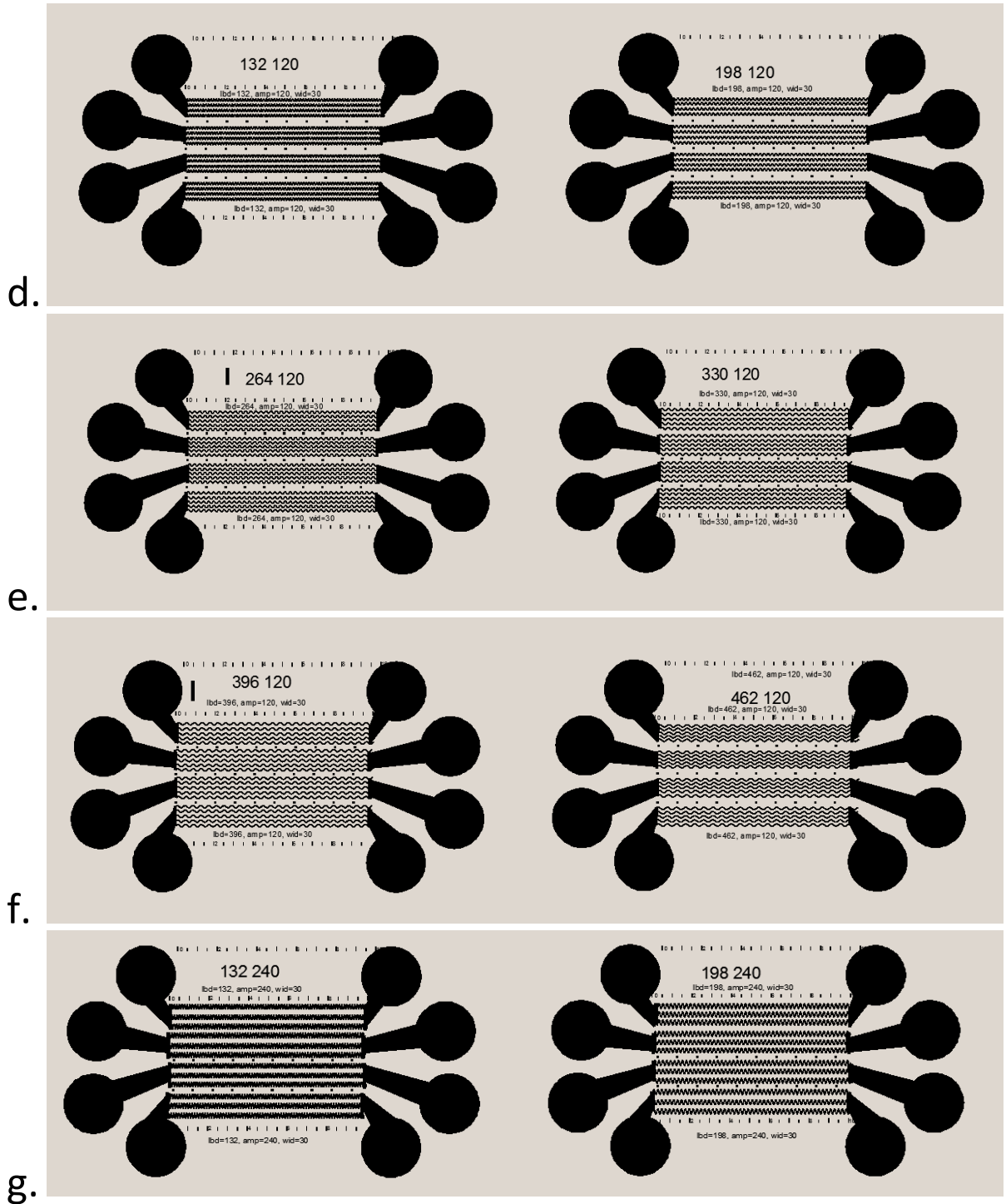
For every tracked worm, the output file includes the following: sequential x-y position coordinates, instantaneous velocity at each position, number of halts and reversals, and instantaneous locomotion amplitude and wavelength. The parameter extraction is made adaptable to different nematode species by a preset pixel range specified by the user. In addition, the user is able to provide the program with information about regions of interest in the recorded videos. This allows the user to safely ignore irrelevant data, shorten execution time, and use separate sets of data from parallel experiments.



## Appendix 2

### Mask Designs for Sine-wave Channels





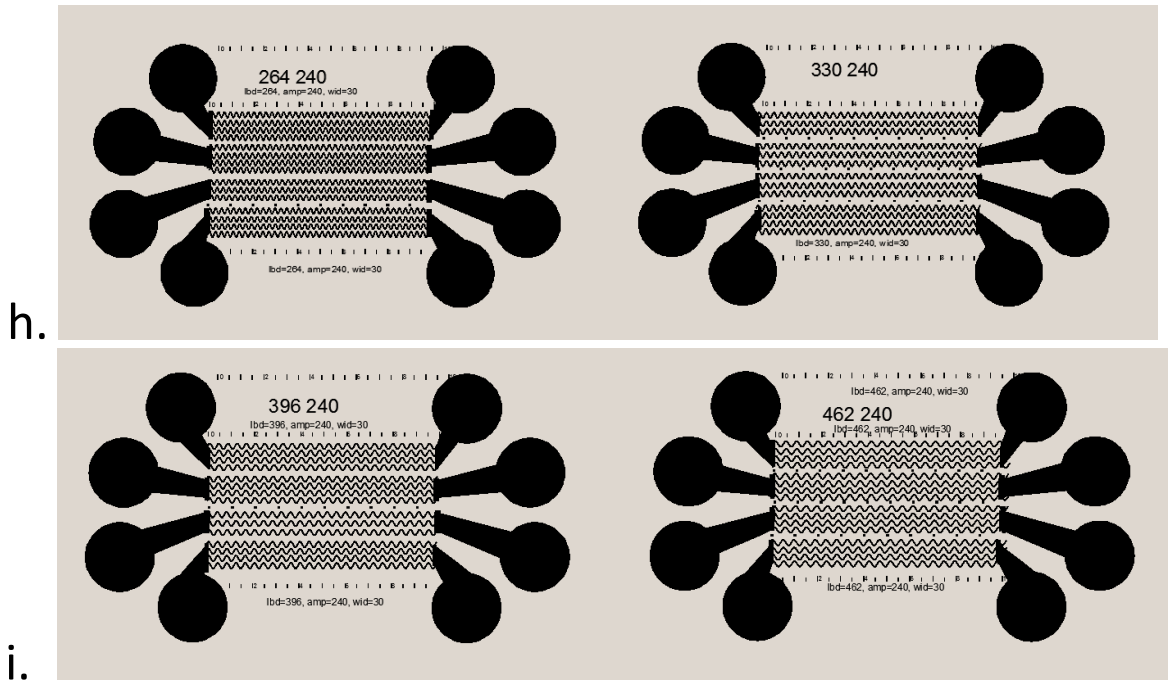


Figure A2.1 (a, b, c, d, e, f, g, h, i): Snapshots of fixed sinusoidal channels tested in Chapter 3

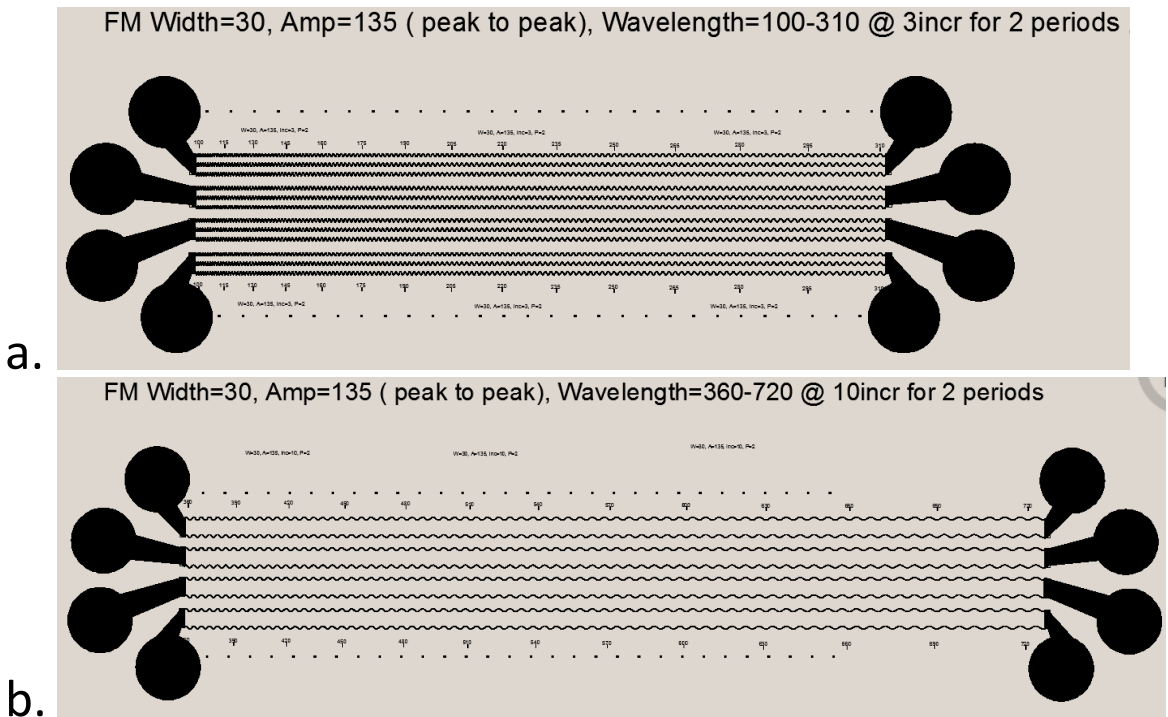
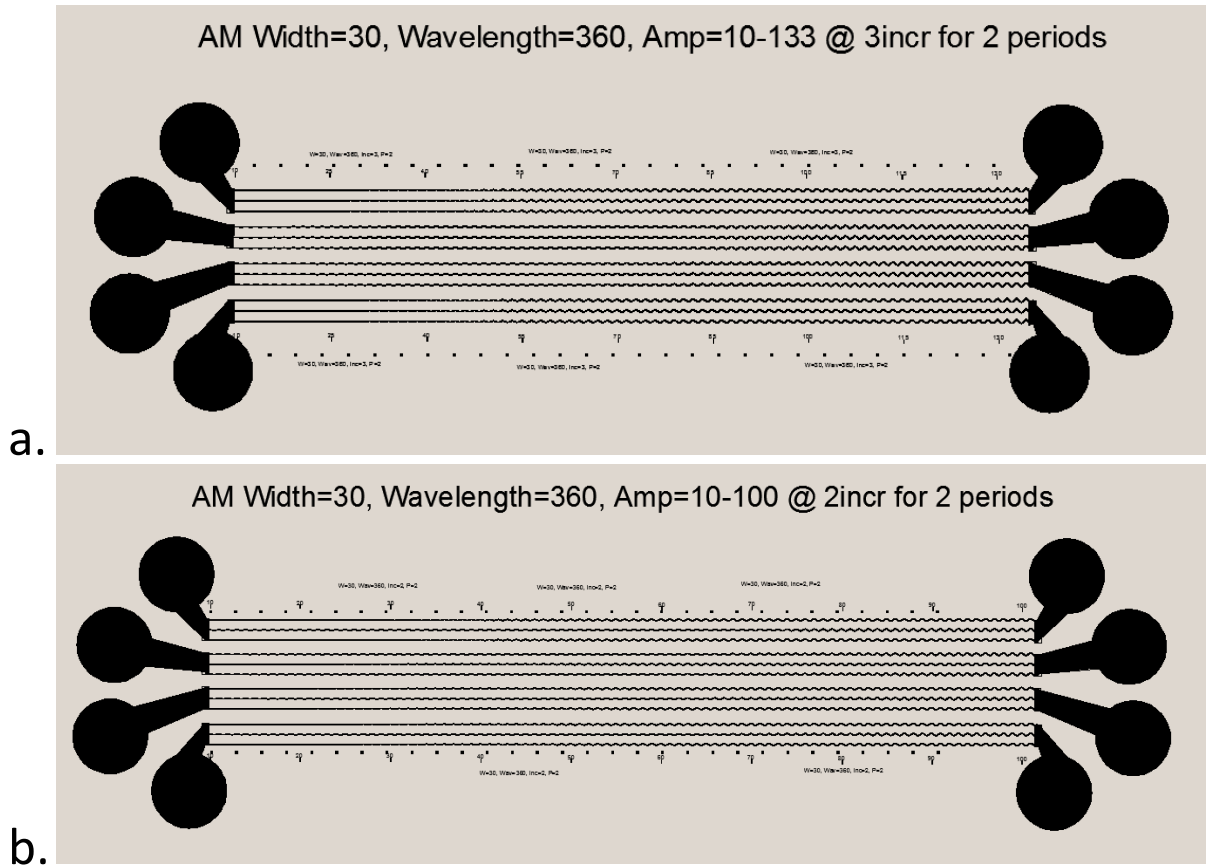


Figure A2.2 (a, b) Snapshots of the amplitude modulated sinusoidal wave channels



**Figure A2.3:** (a, b) Snapshot of the wavelength modulated sinusoidal wave channels

## Appendix 3

### Publications and Awards

#### Publications

- John Carr, Archana Parashar, Baozhen Chen, Alan P. Robertson, Richard J. Martin and Santosh Pandey, “A microfluidic platform for high-sensitivity, real-time drug screening on *C. elegans* and parasitic nematodes”, submitted to *Lab on a Chip*, October 2010
- Baozhen Chen, John Carr, Archana Parashar and Santosh Pandey, “Scalable, CMOS-compatible floating-gate FET for detection of charged biochemical molecules”, submitted to *IEEE Electron Device Letter*, October 2010
- Baozhen Chen, Alex Deutmeyer, John Carr, Alan Robertson, Richard Martin and Santosh Pandey, “Microfluidic bioassay to characterize parasitic nematode phenotype and anthelmintic resistance”, *Parasitology*, doi:10.1017/S0031182010001010, Available on July 2010
- Baozhen Chen, Chengwu Tao and Santosh Pandey, “Biochemical Sensing of Charged Polyelectrolytes with a CMOS Floating-gate Device Architecture”, *IEEE International Conference on Electro/Information Technology*, Ames, IA, 2008
- Baozhen Chen, Chengwu Tao and Santosh Pandey, “Fabrication and Characterization of a Novel Dual-Gate Charge-Sensing Device for Single Cell Studies”, *Material Research Society Spring Meeting*, San Francisco, CA, 2008

- Santosh Pandey, Baozhen Chen and Chengwu Tao, “Novel Neuromorphic CMOS Device Array for Biochemical Charge Sensing”, *IEEE Engineering in Medicine and Biology Society Meeting*, Vancouver, Canada, 2008
- Chengwu Tao, Baozhen Chen and Santosh Pandey, “A novel floating gate biosensing device with controlled charge-modulation”, *IEEE/NIH Life Science Systems and Applications Workshop*, Washington, D. C., 2007

### **Awards**

- Best student/post doctoral paper award, IEEE LISSA workshop, Washington, DC, September 2007
- Best paper award, IEEE International Conference on Electro/Information Technology Ames, IA, May 2008

## **Acknowledgements**

I would like to take this opportunity to express my sincere gratitude to people who helped me during my stay at Iowa State University. Their guidance, support and cooperation were valuable to the successful completion of my graduate studies. First of all, I thank my advisor, Prof. Santosh Pandey for his instruction and advice during my Ph.D. project. I am thankful to my all my Committee Members for their suggestions in this thesis. Prof. Richard Martin and Prof. Alan Robertson have provided valuable guidance in working with nematodes. I am also grateful to my fellow students, Prof. Liang Dong and Prof. Jaeyoun Kim for assisting me in establishing various fabrication protocols. The Microelectronics Research Center has provided facilities for device fabrication. Last but not the least, I am grateful to my parents and family for their cherished love and support.